



The Gemini Planet Imager View of the HD 32297 Debris Disk

Gaspard Duchêne^{1,2}, Malena Rice³, Justin Hom⁴, Joseph Zalesky⁴, Thomas M. Esposito¹, Maxwell A. Millar-Blanchaer⁵, Bin Ren^{6,7,8}, Paul Kalas^{1,9,10}, Michael P. Fitzgerald¹¹, Pauline Arriaga¹¹, Sebastian Bruzzone¹², Joanna Bulger¹³, Christine H. Chen⁷, Eugene Chiang^{1,14}, Tara Cotten¹⁵, Ian Czekala^{1,36}, Robert J. De Rosa¹⁶, Ruobing Dong¹⁷, Zachary H. Draper^{17,18}, Katherine B. Follette¹⁹, James R. Graham¹, Li-Wei Hung¹¹, Ronald Lopez¹¹, Bruce Macintosh¹⁶, Brenda C. Matthews^{17,18}, Johan Mazoyer²⁰, Stan Metchev^{12,21}, Jennifer Patience⁴, Marshall D. Perrin⁷, Julien Rameau²², Inseok Song¹⁵, Kevin Stahl¹¹, Jason Wang^{1,8}, Schuyler Wolff²³, Ben Zuckerman¹¹, S. Mark Ammons²⁴, Vanessa P. Bailey⁵, Travis Barman²⁵, Jeffrey Chilcote^{16,26}, Rene Doyon²², Benjamin L. Gerard^{17,18}, Stephen J. Goodsell²⁷, Alexandra Z. Greenbaum²⁸, Pascale Hibon²⁹, Patrick Ingraham³⁰, Quinn Konopacky³¹, Jérôme Maire³¹, Franck Marchis⁹, Mark S. Marley³², Christian Marois^{17,18}, Eric L. Nielsen^{9,16}, Rebecca Oppenheimer³³, David Palmer²⁴, Lisa Poyneer²⁴, Laurent Pueyo⁷, Abhijith Rajan⁷, Fredrik T. Rantakyö²⁹, Jean-Baptiste Ruffio¹⁶, Dmitry Savransky³⁴, Adam C. Schneider⁴, Anand Sivaramakrishnan⁷, Rémi Soummer⁷, Sandrine Thomas³⁰, and Kimberley Ward-Duong³⁵

¹ Astronomy Department, University of California, Berkeley, CA 94720, USA; gduchene@berkeley.edu

² Université Grenoble Alpes/CNRS, Institut de Planétologie et d'Astrophysique de Grenoble, F-38000 Grenoble, France

³ Department of Astronomy, Yale University, New Haven, CT 06511, USA

⁴ School of Earth and Space Exploration, Arizona State University, P.O. Box 871404, Tempe, AZ 85287, USA

⁵ NASA Jet Propulsion Laboratory, California Institute of Technology, Pasadena, CA 91109, USA

⁶ Department of Physics and Astronomy, Johns Hopkins University, Baltimore, MD 21218, USA

⁷ Space Telescope Science Institute, 3700 San Martin Drive, Baltimore, MD 21218, USA

⁸ Department of Astronomy, California Institute of Technology, 1216 East California Boulevard, Pasadena, CA 91125, USA

⁹ SETI Institute, Carl Sagan Center, 189 Bernardo Avenue, Mountain View, CA 94043, USA

¹⁰ Institute of Astrophysics, FORTH, GR-71110 Heraklion, Greece

¹¹ Department of Physics & Astronomy, 430 Portola Plaza, University of California, Los Angeles, CA 90095, USA

¹² Department of Physics and Astronomy, Centre for Planetary Science and Exploration, The University of Western Ontario, London, ON N6A 3K7, Canada

¹³ Pan-STARRS Observatory, Institute for Astronomy, University of Hawai'i, 2680 Woodlawn Drive, Honolulu, HI 96822, USA

¹⁴ Earth and Planetary Science Department, University of California, Berkeley, CA 94720, USA

¹⁵ Physics and Astronomy, University of Georgia, 240 Physics, Athens, GA 30602, USA

¹⁶ Kavli Institute for Particle Astrophysics and Cosmology, Stanford University, Stanford, CA 94305, USA

¹⁷ University of Victoria, 3800 Finnerty Road, Victoria, BC, V8P 5C2, Canada

¹⁸ National Research Council of Canada Herzberg, 5071 West Saanich Road, Victoria, BC V9E 2E7, Canada

¹⁹ Physics and Astronomy Department, Amherst College, 21 Merrill Science Drive, Amherst, MA 01002, USA

²⁰ LESIA, Observatoire de Paris, Université PSL, CNRS, Sorbonne Université, Université Paris Diderot, Sorbonne Paris Cité, 5 place Jules Janssen, F-92195 Meudon, France

²¹ Department of Physics and Astronomy, Stony Brook University, Stony Brook, NY 11794-3800, USA

²² Institut de Recherche sur les Exoplanètes, Département de Physique, Université de Montréal, Montréal, QC, H3C 3J7, Canada

²³ Leiden Observatory, Leiden University, P.O. Box 9513, 2300 RA Leiden, The Netherlands

²⁴ Lawrence Livermore National Laboratory, 7000 East Avenue, Livermore, CA 94550, USA

²⁵ Lunar and Planetary Laboratory, University of Arizona, Tucson, AZ 85721, USA

²⁶ Department of Physics, University of Notre Dame, 225 Nieuwland Science Hall, Notre Dame, IN 46556, USA

²⁷ Gemini Observatory, 670 N. A'ohoku Place, Hilo, HI 96720, USA

²⁸ Department of Astronomy, University of Michigan, Ann Arbor, MI 48109, USA

²⁹ Gemini Observatory, Casilla 603, La Serena, Chile

³⁰ Large Synoptic Survey Telescope, 950N Cherry Avenue, Tucson, AZ 85719, USA

³¹ Center for Astrophysics and Space Science, University of California San Diego, La Jolla, CA 92093, USA

³² Space Science Division, NASA Ames Research Center, Mail Stop 245-3, Moffett Field, CA 94035, USA

³³ Department of Astrophysics, American Museum of Natural History, New York, NY 10024, USA

³⁴ Sibley School of Mechanical and Aerospace Engineering, Cornell University, Ithaca, NY 14853, USA

³⁵ Five College Astronomy Department, Amherst College, Amherst, MA 01002, USA

Received 2020 February 11; revised 2020 March 25; accepted 2020 April 3; published 2020 May 7

Abstract

We present new *H*-band scattered light images of the HD 32297 edge-on debris disk obtained with the Gemini Planet Imager. The disk is detected in total and polarized intensity down to a projected angular separation of 0'' 15, or 20 au. On the other hand, the large-scale swept-back halo remains undetected, likely a consequence of its markedly blue color relative to the parent body belt. We analyze the curvature of the disk spine and estimate a radius of ≈ 100 au for the parent body belt, smaller than past scattered light studies but consistent with thermal emission maps of the system. We employ three different flux-preserving post-processing methods to suppress the residual starlight and evaluate the surface brightness and polarization profile along the disk spine. Unlike past studies of the system, our high-fidelity images reveal the disk to be highly symmetric and devoid of morphological and surface brightness perturbations. We find the dust scattering properties of the system to be consistent with those observed in other debris disks, with the exception of HR 4796. Finally, we find no direct evidence for the presence of a planetary-mass object in the system.

Unified Astronomy Thesaurus concepts: Debris disks (363); Circumstellar dust (236)

³⁶ NASA Hubble Fellowship Program Sagan Fellow.

1. Introduction

Debris disks represent a late stage in planetary system evolution, after most of the gaseous component of the protoplanetary disk has dissipated. Remnant planetesimals are thought to collide and continuously replenish these disks with small dust grains (Wyatt 2008). Debris disks are characterized by low integrated fractional luminosity ($\tau_{\text{IR}} = L_{\text{IR}}/L_{\text{bol}} \lesssim 0.01$), indicating that these are generally optically thin. While challenging, imaging these disks in scattered light in the optical and/or near-infrared often reveals offsets, asymmetries, and other irregularities, which provide a unique lens to study mature planetary systems. This is best illustrated by the β Pic system, the first debris disk ever imaged in which a gas giant planet responsible for a noticeable disk warp was subsequently discovered (Smith & Terrile 1984; Burrows et al. 1995; Lagrange et al. 2009). To date, over three dozen debris disks have been imaged in scattered light, although image fidelity is often limited by artifacts introduced by the necessary suppression of the remaining glare of the central star (Hughes et al. 2018).

HD 32297 is a young (≤ 30 Myr Kalas 2005), A6 star³⁷ located 133 pc away from the Sun³⁸ (Brown et al. 2018). It has one of the largest infrared excesses observed among main-sequence stars ($\tau_{\text{IR}} \gtrsim 3 \times 10^{-3}$, Silverstone 2000) and, as a result, it is one of the best studied debris disk systems to date. In particular, it has been spatially resolved in scattered light from the optical to $4 \mu\text{m}$ (e.g., Kalas 2005; Schneider et al. 2005; Rodigas et al. 2014), as well as in thermal emission in the mid-infrared (Fitzgerald et al. 2007; Moerchen et al. 2007) and at millimeter wavelengths (Maness et al. 2008; MacGregor et al. 2018). No planet has been detected in the system, down to sensitivities of $\approx 2\text{--}5 M_{\text{Jup}}$ (Bhowmik et al. 2019). In addition to a copious amount of dust, the HD 32297 disk is remarkable because of the detection of Na I absorption (with five times the column density observed in β Pic; Redfield 2007) as well as atomic and molecular gas emission (Donaldson et al. 2013; Greaves et al. 2016; MacGregor et al. 2018; Cataldi et al. 2020). While the number of gas detections in the debris disks is steadily rising (Hughes et al. 2018), the HD 32297 system stands out as one of the most prominent of such systems. The origin of this gas is still debated, but it is likely released during collisions between planetesimals, possibly very recently (Kral et al. 2017; Cataldi et al. 2020).

Resolved images of the HD 32297 debris disk revealed two spatially distinct components: a parent body belt and an extended outer halo. The halo, which was the first component detected in scattered light (Kalas 2005), extends to at least 1800 au (Schneider et al. 2014) and displays an unusually curved morphology that may be indicative of interaction with the interstellar medium (Debes et al. 2009), with an undetected planet (Lee & Chiang 2016), with the gas component of the disk (Lin & Chiang 2019), or of a recent collision in the disk, as proposed by Mazoyer et al. (2014) to explain a similar structure in the HD 15115 disk. Either way, the halo is thought to be populated by the smallest dust grains produced by

collisions in the parent belt and that are subsequently placed in high-eccentricity orbits through radiative forces.

The parent body belt, which is seen nearly exactly edge-on, has a radius of about 110–130 au in scattered light (e.g., Boccaletti et al. 2012; Esposito et al. 2014; Bhowmik et al. 2019). Images are consistent with a sharp-edged inner cavity inside of this radius, while the surface density drops smoothly outwards to form the halo. This belt radius coincides with the value derived from thermal emission maps (Moerchen et al. 2007); although, the superior sensitivity of ALMA recently showed that the belt is radially extended and that the halo also contributes to the millimeter emission (MacGregor et al. 2018). Several lateral asymmetries and substructures have been proposed in scattered light images of the main belt (Currie et al. 2012; Asensio-Torres et al. 2016). These studies are generally hampered by the necessity to employ aggressive point-spread function (PSF) subtraction methods that often introduce spurious features, however, and the reality of these features remains to be firmly established (e.g., Milli et al. 2012).

Many of the studies discussed above have attempted to reproduce observations of the HD 32297 disk to infer its dust properties. In part because each study considers different data sets (scattered light images, thermal emission maps, and entire spectral energy distributions), no consensus has been reached regarding the minimum grain size in the parent body belt. It could be sub-micron (Fitzgerald et al. 2007; Esposito et al. 2014; Bhowmik et al. 2019), thus, likely smaller than the blowout size, or as large as several microns, albeit possibly with high porosity (Donaldson et al. 2013; Rodigas et al. 2014). The only firmly established conclusion is that the dust is strongly forward scattering, both in the optical and the near-infrared. The composition of the dust is equally contentious, ranging from a rather standard mixture of astrophysical material to pure water ice. In principle, the recent measurement of the scattered light polarization fraction in the system (Asensio-Torres et al. 2016) should help reduce ambiguities, but the quality of this data set was too low to warrant detailed modeling.

Here, we present new scattered light observations of the central (< 250 au) regions of the HD 32297 debris disk using the polarimetric mode of the high-contrast Gemini Planet Imager (GPI; Macintosh et al. 2014). We present high-fidelity scattered light images of the parent body belt in both total and polarized intensity. This allows us to assess the belt’s overall geometry and to empirically characterize its dust scattering properties (Section 3). We then use these quantities to constrain the properties of the dust contained in the belt in Section 4. In Section 5, we discuss the implications of our findings before concluding in Section 6.

2. Observations and Data Reduction

On 2014 December 18 (UT), we observed HD 32297 with GPI’s polarimetric mode in the H band with a $0''.24$ -diameter occulting mask. We obtained thirty-eight 60 s frames with a half-wave plate cycling through position angles 0° , 22.5° , 45° , and 67.5° . The observations were acquired at an airmass of 1.27 and through the target’s transit, resulting in a total field rotation of 19° . Conditions were somewhat poorer than average, with seeing estimates of $1''.17$ and $0''.82$ from the Gemini Differential Image Motion Monitor and the Multi-Aperture Scintillation Sensor, respectively. Telemetry from the AO

³⁷ The oft-quoted A0 spectral for HD 32297, which can be traced back to the Henry Draper catalog, has been conclusively shown to be too hot; the best-fitting effective temperature for the stars is in the 7600–8000 K range (Fitzgerald et al. 2007; Rodigas et al. 2014).

³⁸ All physical lengths quoted in this paper are based on this distance, which is significantly larger than the Hipparcos distance used in previous studies (Perryman et al. 1997).

system (Poyneer et al. 2014; Bailey et al. 2016) reported post-correction wave front residuals of 150–160 nm.

The data were processed using the GPI Data Reduction Pipeline v1.3 (Maire et al. 2012; Perrin et al. 2014). The raw data were dark subtracted, flat-fielded, cleaned of correlated detector noise, bad pixel corrected, flexure corrected, and combined into a polarization datacube (where the third dimension holds two orthogonal polarization states). Each datacube was then corrected for non-common path errors via a double differencing algorithm (Perrin et al. 2015). The star location was determined from the satellite spots using a radon-transform-based algorithm (Wang et al. 2014). The instrumental polarization was estimated by measuring the apparent stellar polarization in each polarization datacube as the mean normalized difference of pixels within 20 pixels from the star’s location. The estimated instrumental polarization was then subtracted from each pixel, scaled by the pixel’s total intensity (Millar-Blanchaer et al. 2015). While the region used to estimate the instrumental polarization includes some signal from the disk itself, only a small fraction of all pixels are affected by it, and, out to that radius, the residual starlight is brighter than the disk itself. We thus estimate that this does not lead to a significant bias. The data cubes were then smoothed with a Gaussian kernel (FWHM of 1 pixel), rotated to a common orientation, and combined into Stokes data cubes via singular value decomposition (Perrin et al. 2015). Finally, the $[I, Q, U, V]$ Stokes cube was converted to the $[I, Q_\phi, U_\phi, V]$ “radial Stokes” cube (Schmid et al. 2006), with the convention that positive Q_ϕ indicates a polarization vector that is perpendicular to the line joining a given point in the image to the star location, while U_ϕ represents polarization vectors oriented at 45° from this line.

The data were flux calibrated by measuring the brightness of the reference satellite spots (Hung et al. 2015; Esposito et al. 2020). The HD 32297 disk overlaps with two of the four spots in some images, introducing a potential for a biased calibration. We therefore estimated the ADU-to-Jy conversion factors using the latter 10 frames of the sequence, in which all satellite spots are cleanly separated from the disk, and we assumed that the same factors applied to the first half of the sequence. From the scatter across data cubes, the flux calibration factor is measured with a 5% uncertainty.

3. Observational Results

3.1. Raw Images

The HD 32297 disk is bright enough to be detected in raw individual frames, as illustrated in Figure 1(a). In the combined Stokes I image (Figure 1(b)), the disk is strongly detected above the background of the PSF halo outside of $\approx 0''.3$, although measuring accurate surface brightness still requires an additional step of PSF subtraction; this is performed in Section 3.2.

Because light from the star is intrinsically unpolarized, there is no leftover halo in the Stokes Q_ϕ and U_ϕ images. In the former, the disk is strongly detected from just outside the edge of the coronagraphic mask ($\approx 0''.15$) out to a sensitivity-limited distance of about $1''.2$ from the star. This data set provides the smallest stellocentric distance at which the disk is clearly detected to date. Under the assumption of single scattering as in the optically thin regime, U_ϕ should be null throughout the image (Canovas et al. 2015). This is true outside of $0''.25$,

where we use the U_ϕ map to evaluate the noise associated with the Q_ϕ map by measuring the standard deviation in concentric annuli. In the inner region, however, a U_ϕ signal is observed at approximately the same location as the disk at a level of 5%–10% of the Q_ϕ signal. This could either be a consequence of multiple scattering, implying that the disk is not quite optically thin, or an indication of uncorrected polarization systematics. Because the strongest signal in the U_ϕ map is offset by about 2 pixels perpendicular to the disk major axis from the strongest Q_ϕ signal, we deem the latter interpretation as likely correct. Despite various attempts to improve data reduction, we could not find a satisfactory method to fully remove this artifact. We thus evaluate the uncertainty associated with the Q_ϕ map with the same method at these inner regions as at larger radii, noting that this may introduce a bias because the dispersion between pixels within annuli is not driven by random noise.

3.2. Total Intensity Image: PSF Subtraction

To more clearly reveal the HD 32297 disk in total intensity, it is necessary to subtract the residual starlight in the Stokes I image. As in previous GPIES disk analyses (e.g., Kalas et al. 2015; Draper et al. 2016), we implemented several independent methods, each with their own advantages and limitations. The resulting PSF-subtracted images are presented in the top row panels of Figure 2.

First, we used a standard Angular Differential Imaging (ADI) approach with `pyKLIP-ADI` (Wang et al. 2015), a custom implementation of the KLIP algorithm (Soummer et al. 2012). This method is highly effective for point source discovery but results in systematic self-subtraction of extended objects such as disks. In the particular situation of edge-on disks, strong negative “wings” are imprinted on each side of the disk, especially when the total field rotation is modest as is the case here. To minimize self-subtraction, we adopted a conservative set of parameters, using only 5 KL modes and averaging images with 3–9 annuli. In the resulting image, the disk is traced all of the way to the coronagraphic mask, with an apparently smooth brightness profile.

To mitigate self-subtraction, we also used `pyKLIP` with Reference Differential Imaging (RDI). Here, we first assemble a library of nearly 25,000 H -band images of stars observed with GPI, from which frames with known astrophysical signals or instrumental issues were removed. We then select the 500 images that are most highly correlated with each individual frame of HD 32297. The PSF is then estimated by applying the same KLIP process as above to this set of reference images. While this approach prevents self-subtraction, `pyKLIP-RDI` can still suffer from over-subtraction, as any astrophysical signal can be misinterpreted as a PSF “feature” by the algorithm. This is particularly relevant in the case of a bright disk like HD 32297, where the ratio of disk-to-PSF signal approaches or even exceeds unity in some parts of the image. We thus employed a conservative set of parameters (5 KL modes, averaged over 3–9 annuli, 500 reference PSFs chosen). Despite significant, low-frequency background fluctuations in the resulting image, the disk is clearly detected at all radii outside of the coronagraphic mask.

To sidestep self- and over-subtraction in a different way, we also employed the mask-and-interpolate (MI) PSF subtraction at the single-frame level (Perrin et al. 2015). We first mask out a 15 pixel high box centered on the disk, as well as the four satellite spots. The masked pixels are then replaced with the

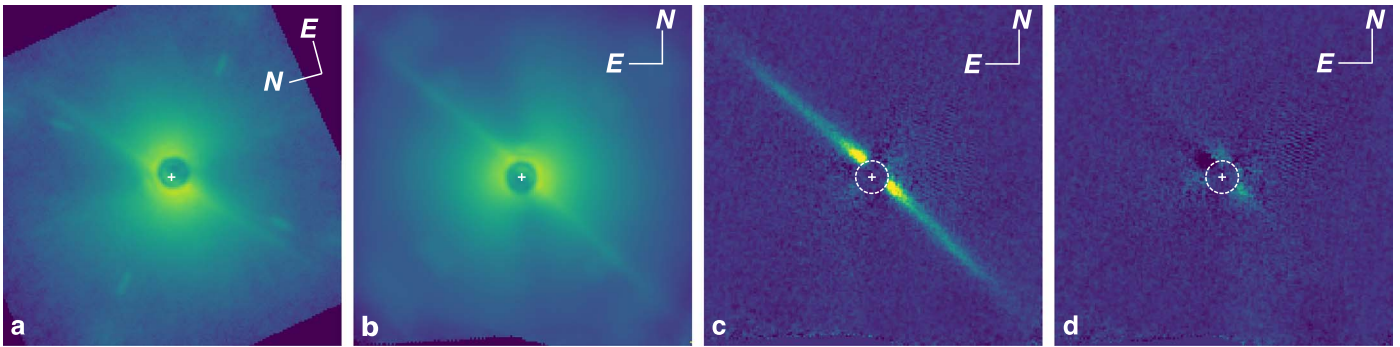


Figure 1. GPI H -band total intensity images of HD 32297. A single frame and the complete sequence total intensity images are shown on the same logarithmic stretch in panels (a) and (b), respectively. The two right-hand side panels present the Stokes Q_ϕ , panel (c) and U_ϕ , panel (d) polarized intensity images, respectively, with both shown on the same linear stretch from -5 to 30 times the background noise ($0.2 \text{ mJy arcsec}^{-2}$). Each panel is $2''.5$ on a side, and the white plus symbol indicates the location of the star. The size of the focal plane mask is indicated by a dashed circle in panels (c) and (d). Panels (b)–(d) are shown with the same orientation, while panel (a) is shown with the orientation of that particular frame. The reference compass rose segments have length $0''.25$.

result of interpolating through the neighboring unmasked pixels with a fourth-order polynomial function. The resulting image is then smoothed with a 13 pixel ($\approx 0''.18$) running median box to only model the low spatial frequency component of the PSF, and it is subsequently subtracted from the original frame. Residual fluctuations in the background are significantly lower than in the RDI case, except close to the inner working angle where the interpolation scheme fails to reproduce the sharp intensity gradients of the PSF. The region interior of $\approx 0''.25$ from the star is too uncertain to consider in our subsequent analysis, but the disk is strongly detected outside of this radius.

Finally, we applied the Nonnegative Matrix Factorization (NMF) method as implemented within `pyKLIP`. NMF is an iterative method based on the decomposition of the PSF into separate components that only contain positive pixels (Ren et al. 2018). Similar to the RDI process, we selected the 500 most correlated frames in the library of GPI images and used the first five modes computed by NMF to subtract the PSF. The resulting total intensity image for HD 32297 reveals a smooth brightness profile, albeit with leftover background fluctuations that are intermediate in strength between the RDI and MI methods. Like the ADI and RDI methods, the NMF method yields a strong detection of the disk all of the way to the edge of the coronagraphic mask.

Apart from the bright disk, all four PSF-subtracted images are marked by a diagonal negative residual pattern (along position angles $\sim 15^\circ$ and $\sim 190^\circ$). This likely is a consequence of the “butterfly” structure of the PSF visible in the raw total intensity images (see Figure 1) and that is imparted by winds in the atmosphere (Madurowicz et al. 2019). To improve the quality of the final images, we perform a fourth-order polynomial fit in concentric annuli after masking out a vertical box centered on the disk; to improve the fit, the process handles each side of the disk separately. Effectively, this performs a second mask-and-interpolate subtraction, on a single annuli basis. The resulting images are shown in Figure 2. In the case of the RDI and NMF methods, which are characterized by more structured residuals, the subtraction residuals and amplitude of the background fluctuations become too high to produce a clean image of the disk inside of $0''.3$ from the star. For these images, we do not attempt to measure the absolute brightness of the disk closer in.

3.3. Disk Morphology and Geometry

In both total and polarized intensity, the HD 32297 disk is revealed as a sharp, almost linear feature on each side of the star along position angle (PA; measured in the usual east of north convention) of $47^\circ 90 \pm 0^\circ 17$, as measured from the geometric fit presented below, where the uncertainty incorporates the astrometric calibration precision (De Rosa et al. 2020). As was found in past scattered light images of the system (e.g., Boccaletti et al. 2012), the GPI data reveal that the spine of the disk is not perfectly straight as would be the case for a perfectly edge-on viewing geometry. Instead, the spine is slightly curved and passes to the NW of the star (see Figure 3), indicating that this side is the front side of the disk under the assumption that scattering is preferentially in the forward direction. We find no conclusive evidence of the back side of the disk.

Comparing the PSF-subtracted images of the disk to radiative transfer models can yield simultaneous constraints on both the disk geometry and dust scattering and, thus, physical properties. This is a computationally intensive task and results are often fraught with model-dependent biases and ambiguities, however. To take advantage of the high-fidelity GPI images, we instead adopt a two-step empirical approach. In the first step, we ignore the surface brightness profile along the disk, which is dictated by the surface density and scattering phase function, and focus on the spine morphology to assess the disk geometry. Having established the system geometry, we can then constrain the dust scattering properties. We defer to Section 4 for the interpretation in terms of the physical properties of the dust.

The marked curvature of the spine and the uniform vertical FWHM along the disk spine (see below) are best explained if the disk is radially narrow since a broad ring would yield a smeared appearance due to line-of-sight project effects. This allows us to employ a simple model consisting of a circular ring of radius R_d , whose center can be offset by δ_x from the star along the major axis, and observed with an inclination i . We do not explore the possibility of an offset along the minor axis of the disk as the nearly edge-on configuration of the system renders this effect negligible. To incorporate the halo of blown-out dust to this simple model, we assume that the spine extends horizontally outside the ring ansae, i.e., with no offset from the disk major axis. On the larger scale, the halo is markedly curved, but this effect is only significant outside of the GPI

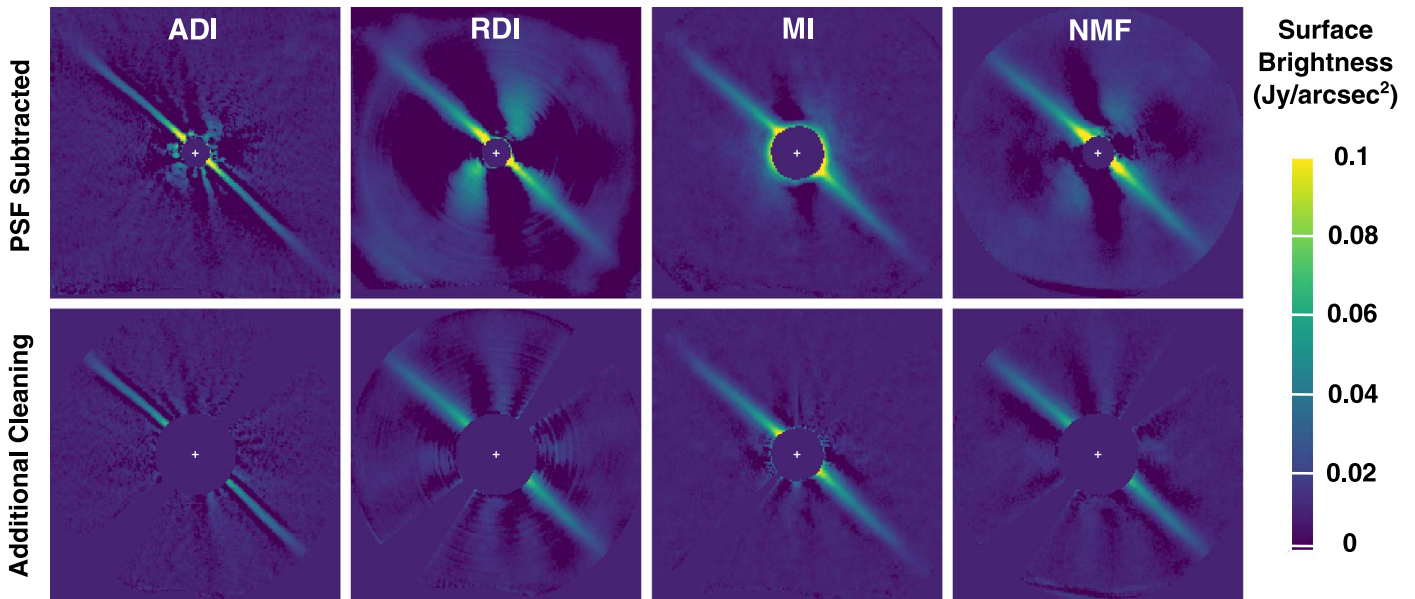


Figure 2. GPI H -band total intensity images of the HD 32297 disk after PSF subtraction, using four different methods. From left to right, the PSF subtraction methods are a conservative ADI-based pyKLIP that only uses images from the target’s sequence, an RDI-based implementation of pyKLIP using other GPI H -band images to evaluate the PSF, a frame-by-frame MI process, and an NMF-based implementation of pyKLIP. The top row panels present the product of each of these processes, whereas the bottom row panels are our final products, after a polynomial fit is performed azimuthally and subtracted to further reduce the background. All images are shown on the same square root stretch from -0.001 to $0.1 \text{ Jy arcsec}^{-2}$, except for the ADI images where the surface brightness has been multiplied by a factor of two to qualitatively offset self-subtraction. All images have a $2''.5$ field of view and are oriented so that north is up and east to the left. Numerical masks have been applied in regions with excessive subtraction residuals.

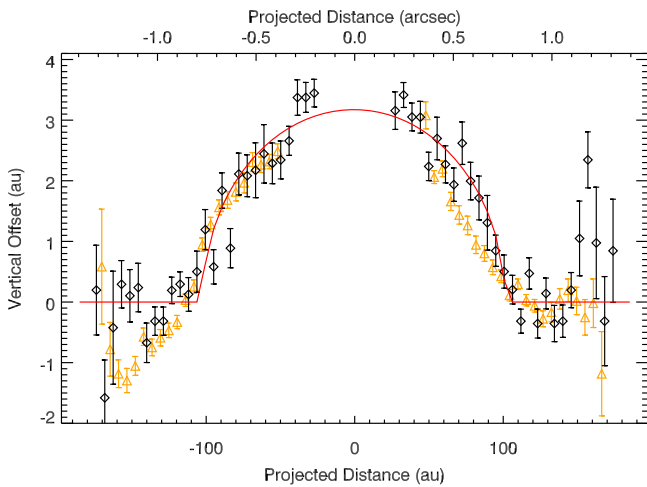


Figure 3. Vertical offset between the spine of the HD 32297 disk and a line at PA $47:9$ passing through the central star. Black diamonds and orange triangles represent estimates based on the polarized intensity and RDI total intensity images, respectively. The latter is representative of all four PSF subtraction methods employed here. The red curve is the inclined ring model that best fits the spine location in the polarized intensity image.

field of view. Implicitly, this model assumes that the disk is an intrinsically narrow ring whose eccentricity is small. For a given PA of the disk major axis and (x_*, y_*) position of the star, we measure the spine by rotating the image so that the disk major axis is horizontal, binning the image by a factor of three (i.e., a resolution element) along the horizontal axis, and fitting a Gaussian function to the intensity profile perpendicular to the disk. Uncertainties are assigned at the pixel level based on the standard deviation in concentric 1 pixel wide annuli and propagated through the Gaussian fit for both of the total intensity maps, thus neglecting residual correlated noise.

To explore the six-dimensional parameter space, we use a Metropolis–Hastings Markov Chain Monte Carlo (MCMC) algorithm. We first perform the fit using the Q_ϕ (hereafter, polarized intensity) image since (1) it provides a clear detection down to a smaller inner working angle, and (2) it is not subject to systematic biases introduced by PSF subtraction. As illustrated in Figure 3, the data are reasonably well fit by this simple model ($\chi^2_{\text{red}} = 2.1$). The resulting model parameters are: $i = 88:21^{+0.06}_{-0.08}$, $R_d = 101.7^{+1.5}_{-2.1} \text{ au}$ and $\delta_x = -0.9^{+1.3}_{-1.5} \text{ au}$. The corresponding posteriors are shown in Figure 4. We find no significant offset between the star and ring center, with a 3σ upper limit on the ring eccentricity of $e < 0.05$, yielding further support to our simple geometric model.

We then applied the same fitting method to each of the four PSF-subtracted images. The resulting posteriors are also shown in Figure 4. For each data set, the posteriors are much narrower than the posteriors from the fit to the polarized intensity image. The total intensity posteriors are also inconsistent with one another. The narrow posteriors are a consequence of the fact that uncertainties are underestimated due to correlated residuals in the PSF-subtracted images. The offsets between the various posteriors are likely a consequence of subtle, but significant, modifications to the disk spine introduced by the PSF subtraction process. To illustrate this point, we show in Figure 3 the spine vertical offset observed in the RDI total intensity image assuming the exact same disk geometric parameters as the best fit to the polarized intensity image. Despite modest deviations from the spine location derived from the polarized intensity image, the fit is much worse ($\chi^2_{\text{red}} = 9.9$), and marginal differences observed on both sides (especially around positions -160 and $+70 \text{ au}$) conspire to push the fit toward significant eccentricity in the ring. Given this experience, we adopt the geometrical parameters obtained from fitting the polarized intensity image.

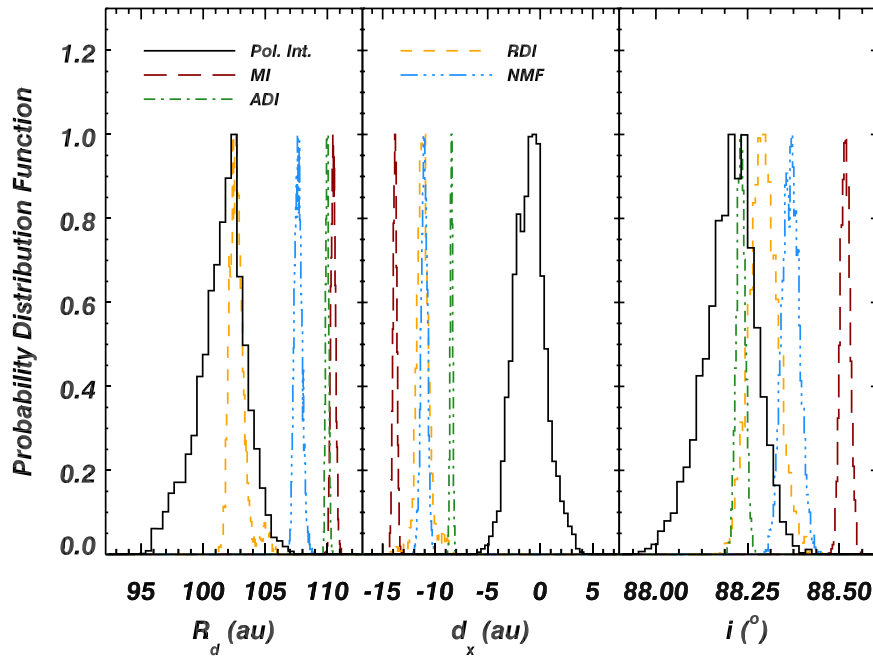


Figure 4. Posterior distributions for the radius, the offset between the ring center and the star, and the inclination of the HD 32297 disk. The solid black histogram represents the fit to the spine as traced in the polarized intensity image, whereas the color histograms are associated with the various PSF subtraction methods used in obtaining the total intensity image (RDI: dashed orange; ADI: dotted-dashed green; MI: long-dashed red; NMF: triple-dotted-dashed blue).

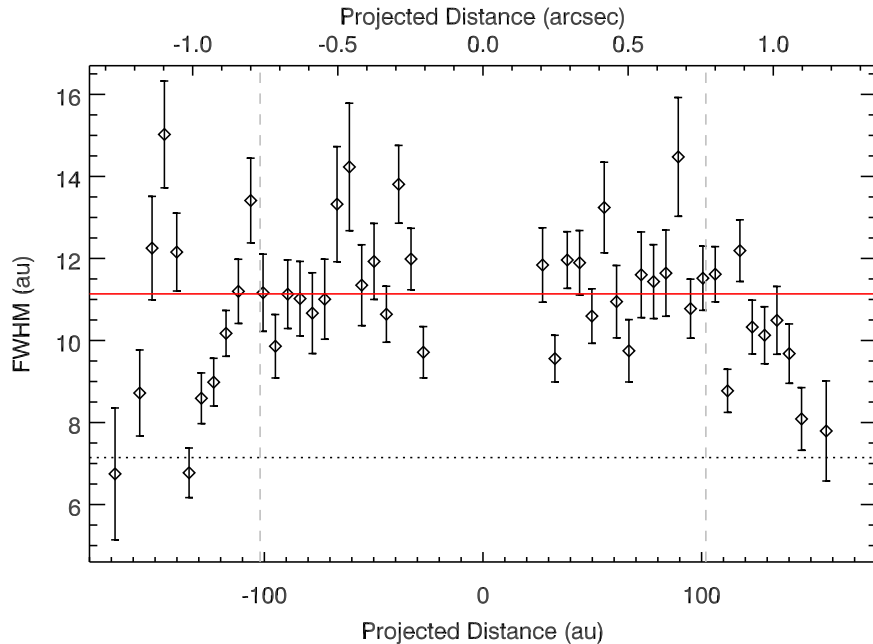


Figure 5. FWHM of the HD 32297 disk in the direction perpendicular to the disk midplane, as measured in the polarized intensity image of the system. The solid red line marks the weighted average over all data points located between the ring ansae (indicated by the vertical dashed lines), whereas the horizontal dotted line represents the intrinsic FWHM of our GPI *H*-band observations.

Overall, while our geometric modeling is in reasonable agreement with past scattered light studies (Boccaletti et al. 2012; Currie et al. 2012; Esposito et al. 2014; Bhowmik et al. 2019), we find a significantly smaller disk radius of ≈ 100 au instead of ≈ 130 au. Most of these studies used total intensity images to assess the ring geometry, thus possibly introducing a systematic bias compared to our analysis of the polarized intensity image of the disk. However, Bhowmik et al. (2019) also analyzed polarized observations and also favor a larger disk radius. Inspection of their Figure 3 reveals a similar shape

for the disk spine as we find here but with a global vertical displacement that can significantly bias the model fitting. This highlights the difficulty in assessing the location of the disk ansae in the edge-on configuration. We defer a more thorough discussion of the disk’s viewing geometry to Section 5.

From the same Gaussian fit as described above, we also measured the vertical FWHM of the disk. The results for the polarized intensity image are shown in Figure 5. After subtracting quadratically the instrumental FWHM from the weighted average over all positions along the disk, we estimate

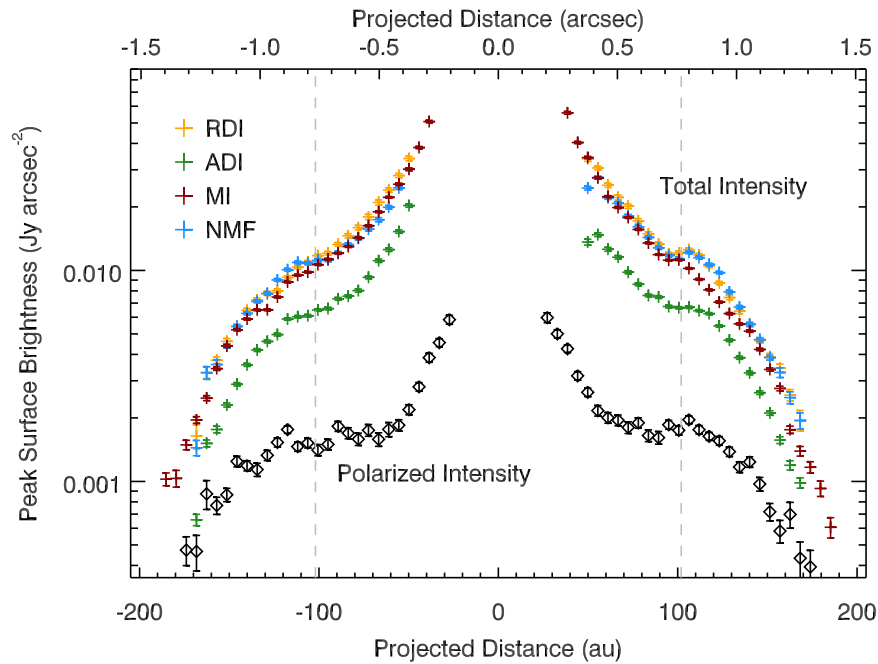


Figure 6. *H*-band surface brightness profiles of the HD 32297 disk in polarized intensity (black diamonds) and total intensity (colored symbols, corresponding of the different PSF subtraction methods). The vertical dashed lines indicate the disk radius as derived from the geometric fit to the disk spine.

the true FWHM of the disk to be about $0''.063$, or 8.3 au. While this is generally consistent with past studies (Boccaletti et al. 2012; Currie et al. 2012; Esposito et al. 2014), we differ from these studies in that we find no significant trend as a function of stellocentric distance. We believe that the trends suggested in past analyses were affected by significant PSF subtraction artifacts. This is further supported by the fact that the FWHM measured with the RDI, MI, and NMF total intensity images shows a significant decline inside of $0''.5$, well below the value measured in the polarized intensity image. The lack of a stellocentric dependency of the disk FWHM is consistent with the hypothesis of a radially narrow disk, as projection effects would result in an increase in FWHM close to the minor axis otherwise.

3.4. Disk Surface Brightness and Polarization Profiles

Except for the ADI method, we have tuned our PSF subtraction methods with an eye toward preservation of the disk surface brightness profile. One of the main motivations to do this was to measure the polarization fraction in the disk. In the Appendix, we show that injecting a model disk into an empty data set and applying the RDI, MI, and NMF methods yields surface brightness profiles that match the injected one to within 10% or better when considering the peak surface brightness along the spine, where PSF subtraction artifacts are smallest. We then proceed to measure the surface brightness profile of the HD 32297 disk using the same Gaussian as used in our geometric analysis. We also note that, since the disk is indeed an optically thin, narrow ring seen almost perfectly edge-on, limb brightening will significantly affect the observed surface brightness close to the ansae. On the other hand, because both total and polarized intensity are affected in a similar way, we expect the polarization fraction map to be mostly free of this effect. Either way, we will take the effect into account in the radiative transfer modeling presented in Section 4.

Figure 6 presents the surface brightness profile in both polarized and total intensity. In total intensity, the profiles measured in the RDI-, MI-, and NMF-processed images agree within $\approx 10\%$ of another, with the exception of a possible local maximum at $\approx 0''.9$ in the MI image (most noticeable on the SW side of the disk). Given the amplitude of differences between the various PSF subtraction methods (and in line with the surface brightness profile obtained by Bhowmik et al. 2019), we consider this feature, which could indicate the ring ansae, as marginally significant at best. The surface brightness profile from the ADI image has a similar shape overall but is $\approx 40\%$ lower than in the other images. Overall, this is consistent with the results of our injection-recovery tests, and the match between the other three methods for the HD 32297 data set provides further confidence in the reliability of the surface brightness profiles derived here.

Both the total and polarized intensity profiles are highly symmetrical about the star, with differences never exceeding 20% at any stellocentric distance. This is in contrast with past claims of significant asymmetries in the inner $1''$ (e.g., Schneider et al. 2005; Currie et al. 2012). Subsequent analyses suggested that PSF subtraction artifacts could be misinterpreted as physical asymmetries (Esposito et al. 2014). In agreement with Bhowmik et al. (2019), we do not recover the local “gaps” observed at $\approx 0''.7$ in total intensity by Asensio-Torres et al. (2016). Instead, the polarized intensity profile plateaus at the location of these putative gaps, and we conclude that the PSF subtraction method employed by these authors amplified these features into apparent surface brightness deficits.

All profiles share a steep decline outside of $\approx 1''$, i.e., in the disk halo. We performed power-law fits and found that the surface brightness profile follows approximately r^{-4} and r^{-5} in polarized and total intensity, respectively. These are in reasonable agreement with previous studies (Boccaletti et al. 2012; Currie et al. 2012; Esposito et al. 2014), although the limited field of view of our observations significantly reduces the precision of our estimates. Inside of a marked inflection

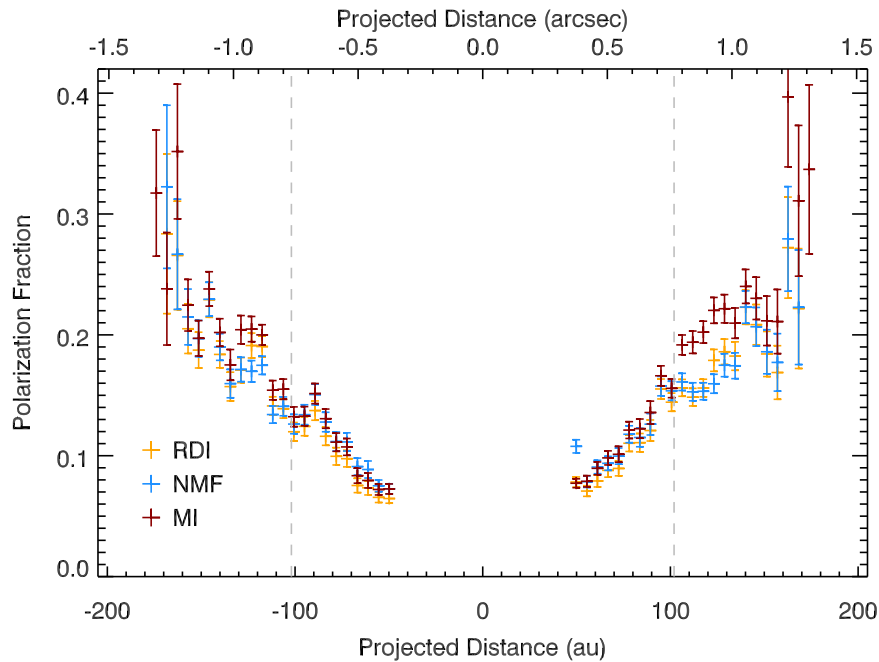


Figure 7. *H*-band polarization fraction across the HD 32297 disk as a function of stellocentric distance. Three of the PSF subtraction methods are used to estimate systematic uncertainties associated with this process. The ADI subtraction is not considered here since it systematically under-evaluates the disk surface brightness. The vertical dashed lines indicate the disk radius as derived from the geometric fit to the disk spine.

point around the disk ansae, the total intensity brightness profile follows $r^{-1.5}$, with suggestive evidence for a gradual steepening toward the smallest projected separations. Again, this is in reasonable agreement with past studies of the system.

Contrary to the total intensity surface brightness profile, the polarized intensity profile displays a broad plateau over the $0''.4$ – $0''.9$ range. The outer edge of this plateau lies ≈ 15 – 20 au outside the ring radius inferred in Section 3.3. This may indicate that the ring has a nonnegligible radial extent, an issue that we will revisit in Section 4. Inside of this plateau, the polarized surface brightness profile follows $r^{-1.5}$, similar to the total intensity profile. While it could be tempting to interpret the break at $0''.4$ as an indication for a secondary ring (with a radius of ≈ 50 au), the absence of any “kink” in the disk spine at that location argues against this scenario. Instead, the central peak in polarized surface brightness must be due instead to sufficiently strong forward scattering to overwhelm the polarization decline inherent to the smallest scattering angles.

Combining the total and polarized intensity surface brightness profile, we compute the polarization fraction along the disk spine. The results are shown in Figure 7. We observe a steady rise, from about 7% at a projected distance of $0''.35$ from the star, to 15% at the ring ansae, and up to 20%–30% at $1''.3$. Our results match well with those obtained by Asensio-Torres et al. (2016). This degree of linear polarization is within the range of near-infrared observations of debris disks (Tamura et al. 2006; Perrin et al. 2015; Draper et al. 2016; Esposito et al. 2018).

To constrain the properties of the dust grains in the HD 32297 disk, we need to extract the scattering phase function (SPF) and the polarizability curves, i.e., the dependency of the total intensity and degree of linear polarization as a function of scattering angle. Under the assumption of a narrow ring, there is a simple analytical transformation between the projected position of a point along the ring spine into a scattering angle. We therefore use the best-fit geometry derived

above from the polarized intensity image to estimate the scattering angle for every point along the spine out to the location of the ring ansae. The resulting curves are shown in Figure 8. One caveat in this process is that close to the ansae, the back side of the disk can contribute significantly to the observed surface brightness since the difference in scattering angle between the front and back side is small, leading to limb brightening. Therefore, we expect that the true SPF of HD 32297 declines more steeply at the largest scattering angles than we measure here. On the other hand, if the polarizability curve is symmetric about 90° (as seen in cometary dust, e.g., Frattin et al. 2019), this effect would cancel out when we compute the polarization fraction, and we thus expect the polarizability curve we derive to be more robust.

The *H*-band SPF we derive for HD 32297, which declines by a factor of about 2.5 between scattering angles 30° and 60° , where contribution from the back side should be minimal based on the disk’s curved spine, is consistent with the nearly universal SPF observed for solar system, debris disks, and protoplanetary disks dust populations (Hughes et al. 2018). On the other hand, it clearly deviates from that observed in the HR 4796 debris disk (Perrin et al. 2015; Milli et al. 2017) as the latter shows a minimum at a scattering angle of $\approx 60^\circ$. There are too few polarizability curves published to date for debris disks to draw a definitive conclusion, but the curve we obtain for HD 32297 is much more consistent with that observed in the HD 35841 system (Esposito et al. 2018) than that in HR 4796 (Perrin et al. 2015).

4. Modeling

We now proceed to evaluate the physical properties of the dust grains: in particular, the grain size distribution and composition (Section 4.1). We then perform a consistency test of our initial narrow ring assumption by directly fitting the disk images based on the derived dust properties (Section 4.2). In

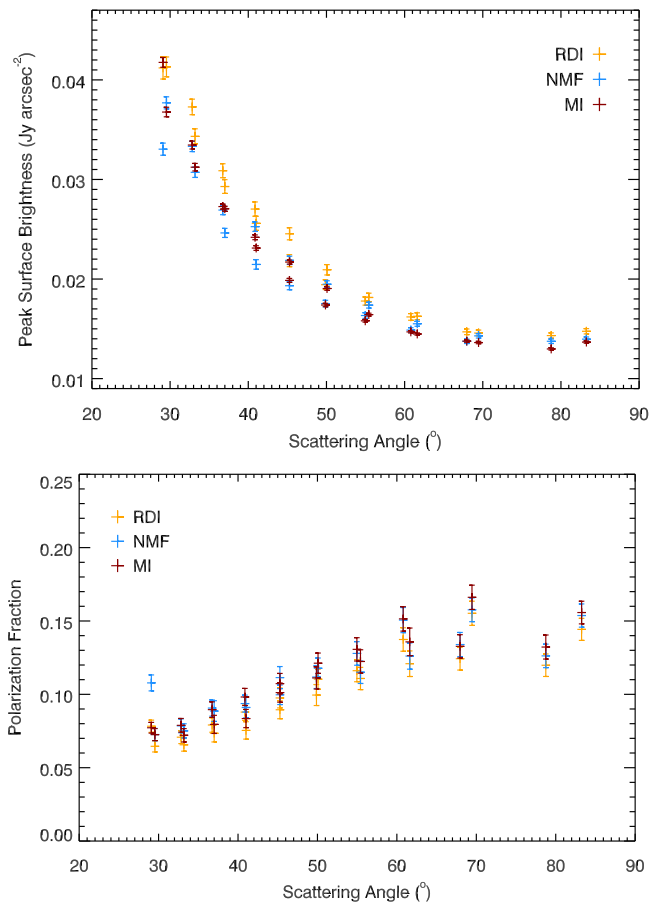


Figure 8. *H*-band SPF (top panel) and polarizability curve (bottom panel) of the HD 32297 disk, using the best estimate of the ring geometry. The color symbols indicate the different PSF subtraction methods. The ADI PSF subtraction is affected by a significant, and likely position-dependent, self-subtraction, which precludes estimating the underlying surface brightness profile without a dedicated forward modeling approach. The two sides of the disk are plotted separately. However, the fact that the best-fit offset of the ring center is small results in nearly identical scattering angles being estimated on each side of the star, except close to the ansae.

principle, a simultaneous fit to the GPI images, with all dust properties and disk geometry parameters left free to vary, represents the most direct approach. However, in cases where models suffer from systematic shortcomings, this can lead to a false sense of success, whereas the multiple-step approach used here allows us to disentangle which assumptions are not verified in our analysis. The general implications of our modeling results are discussed in Section 5.

The NMF, RDI, and MI PSF subtraction methods yield consistent surface brightness profiles and, thus, SPF and polarizability curves. We select the MI-based results for this analysis since they offers the smallest inner working angle. Furthermore, this method intrinsically yields much smaller systematic residuals (see Figure 2), suggesting that the pixel-to-pixel uncertainties are more likely to be mostly random in nature.

4.1. Dust Properties Analysis

4.1.1. Modeling Setup

Here, we wish to reproduce the SPF and polarizability curves derived from our observations of the HD 32297 disk. We adopt

the Mie model, valid for compact, spherical dust grains of homogeneous composition. We note that observations of both laboratory and astrophysical dust populations suggest that this assumption is not optimal (e.g., Pollack & Cuzzi 1980; Hedman & Stark 2015; Milli et al. 2017). However, it is computationally tractable in the context of large dust grains, a problem not yet solved for grain aggregates that are likely to represent a better model of astrophysical dust (e.g., Arnold et al. 2019).

Two components are necessary to build a dust model: the grain size distribution and the dust composition. We follow standard approaches and assume a power-law size distribution, $N(a)da \propto a^{-\eta} da$ ranging from a_{\min} to a_{\max} . Collisional cascade models predict a size distribution with $\eta \approx 3.5$ (e.g., Dohnanyi 1969; Marshall et al. 2017), although deviations from a pure power law are likely (e.g., Thébaud & Augereau 2007). On the other hand, the dust composition is a more challenging issue to handle. It is most often addressed either as a fixed, presupposed composition or as a mixture with variable proportions of several individual compositions (using effective medium theory). While easiest to implement, the first approach can lead to significantly biased results or, worse, a lack of a model that fits the data well if an incorrect composition is picked. The dust mixture suffers from increasing the number of free parameters and, in the worst case scenario, a critical component may be left unexplored. For instance, Rodigas et al. (2015) consider 19 different dust compositions, plus vacuum, to represent porosity, when modeling the HR 4796 debris disk. Even then, only a subset of the data is well fit by the resulting model. To circumvent these issues, we adopt a more direct approach, which consists of fitting for the material’s complex refractive index $m = n + ik$, as this is the quantity from which Mie theory predicts the SPF and polarizability curve. A similar approach was adopted by Graham et al. (2007) in their modeling of the polarized scattered light imaging of the AU Mic debris disk and was instrumental in identifying the need for a large dust porosity in that system.

Because HD 32297 is nearly, but not quite, edge-on, we expect that the back side of the disk contributes to the signal close the ansae. To account for this effect in our models, and taking advantage of the absence of a lateral offset of the central star, we modify the Mie-computed SPF by adding the contributions of the front and back sides using supplementary scattering angles. Similarly, we compute the average of the front and back side polarized intensity signals to obtain the final version of the model polarizability curve. Approximating the disk as being exactly edge-on, we perform this correction at all scattering angles, noting that the correction is only significant close to the ansae. In addition, because monochromatic calculations can experience interference fringes in model SPF and polarizability curves, we compute the Mie models at nine wavelengths spanning the bandpass of the GPI *H*-band filter and average the resulting curves over the wavelength prior to computing the model likelihood. Finally, we normalize all SPFs to their average value in the 40°–60° range of scattering angle in order to focus on the shape of these curves.

We set up three independent parallel-tempered MCMC chains using the `emcee` package (Foreman-Mackey et al. 2013). The first one fits only the HD 32297 SPF, the second only the polarizability curve, and the third fits both curves simultaneously. In all cases, the model likelihood is based on a

Table 1
Best-fitting Dust Properties Based on the SPF Alone, the Polarizability Curve Alone, and Both Curves Simultaneously

Parameter	Prior Range	Best-fitting Model			Median $\pm 1\sigma$			
		SPF	Polar.	Joint	SPF	Polar.	Joint	
							Peak 1	Peak 2
$\log(a_{\min} (\mu\text{m}))$	[-1 .. 1]	-0.08	-0.10	-0.14	$-0.09^{+0.01}_{-0.01}$	$-0.11^{+0.01}_{-0.58}$	$-0.143^{+0.004}_{-0.004}$	$-0.564^{+0.002}_{-0.002}$
$\log(a_{\max} (\mu\text{m}))$	[1 .. 3]	2.84	0.341	2.99	$2.01^{+0.68}_{-0.67}$	$2.07^{+0.61}_{-0.66}$	≥ 2.50	≤ 1.05
η	[2 .. 5]	4.14	3.56	3.52	$4.21^{+0.13}_{-0.13}$	$3.54^{+0.11}_{-0.20}$	$3.516^{+0.008}_{-0.01}$	$3.52^{+0.02}_{-0.02}$
n	[1 .. 5]	3.31	2.64	3.78	$3.30^{+1.07}_{-0.10}$	$4.13^{+0.67}_{-1.51}$	$3.78^{+0.03}_{-0.03}$	$3.49^{+0.06}_{-0.06}$
$\log k$	[-7 .. 1]	-6.16	-1.29	-1.44	≤ -2.83	$-1.37^{+0.11}_{-0.09}$	$-1.44^{+0.01}_{-0.01}$	$-0.77^{+0.02}_{-0.02}$

Note. The range explored for each quantity is indicated in the second column. The upper and lower limits are reported at the 95% confidence level.

standard χ^2 test between the observed and modeled curve. Each of these runs includes 2 temperatures and 50 walkers. Walkers are initially distributed using uniform priors spanning the ranges indicated in Table 1. We remove the first 80% of each chain as a burn-in and use the final 20% to obtain values reported in Table 1, with 1440 iterations kept after burn-in for our SPF fit, 3284 iterations for our polarizability fit, and 3784 iterations for our joint fit. Inspection of the movements of walkers in the parameter space confirm that the chains are well converged.

4.1.2. Results

Our final best-fitting model from each of these runs is displayed in Figure 9, with parameters described in Table 1. While both the observed SPF and polarizability curves are reasonably well reproduced when either quantity is fit separately, the corresponding reduced χ^2 values are 11.8 and 2.3, respectively. These imperfections are driven by the fact that the SPF (and to a lesser degree, the polarizability curve) measured on the NE and SW sides of the disk are formally inconsistent with one another, and the best-fit model is a compromise between both sides. As a result, the formal parameter uncertainties derived from the MCMC process are likely underestimated. Nonetheless, Figure 9 illustrates that our best-fitting models reproduce the overall shape of both the SPF and polarizability curves, suggesting that the values of the best-fitting parameters can be considered as reliable.

Although the model parameters for all three fits (“SPF only,” “polarizability only,” and “joint”) are significantly different, all three model SPFs are similar to the observed one (left panel in Figure 9). This suggests that the SPF of the HD 32297 dust disk is consistent with a large swath of the parameter space, indicating that this quantity has limited discriminatory power as far as dust properties are concerned. This is qualitatively consistent with the observations that many astrophysical dust populations share similar scattering SPFs (Hughes et al. 2018). On the other hand, the polarizability curve may be significantly more constraining, since the “SPF only” dust model is highly inconsistent with the observed polarizability curve. Specifically, due to its much steeper size distribution and very small value of the imaginary part of the refractive index, that model predicts a negative polarization at most relevant scattering angles, i.e., polarization vectors that are radially organized instead of ortho-radial. This is readily excluded by the fact that the Stokes Q_ϕ map shows only a positive signal along the disk. Unsurprisingly, the joint fit resembles the “polarizability only” fit much more than the “SPF only” fit.

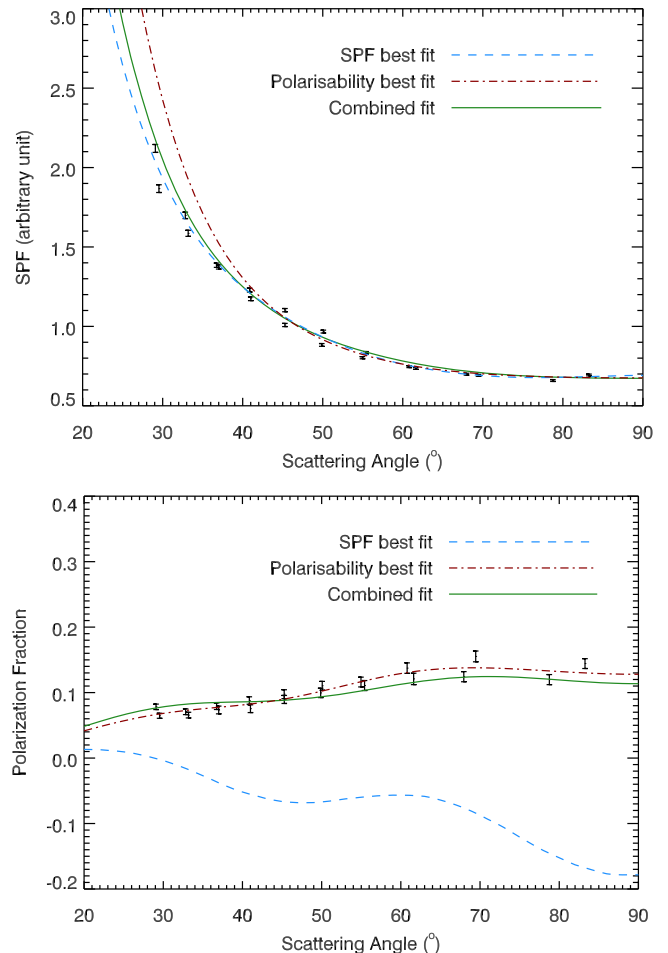


Figure 9. Observed and modeled SPF (top panel) and polarizability (bottom panel) curves. The model curves are modified to account for the superimposition of the front and back sides of the disk. Observed quantities, as derived from the MI total intensity image, are shown as black errorbars while the colored curves represent the best fit to the SPF (red dotted-dashed), to the polarizability curve (blue dashed), and to both curves simultaneously (solid green).

Turning our attention to the best-fitting model parameters, we first note that the “joint” fit leads to two distinct families of models, as illustrated in Figure 10. The family characterized by a large value of a_{\max} , which is referred to as “Peak 1” in Table 1, is consistent with both the “SPF only” and “polarizability” fits, and we thus consider it as the most plausible model. Besides this consistency, the other family of models is characterized by a very narrow grain size distribution

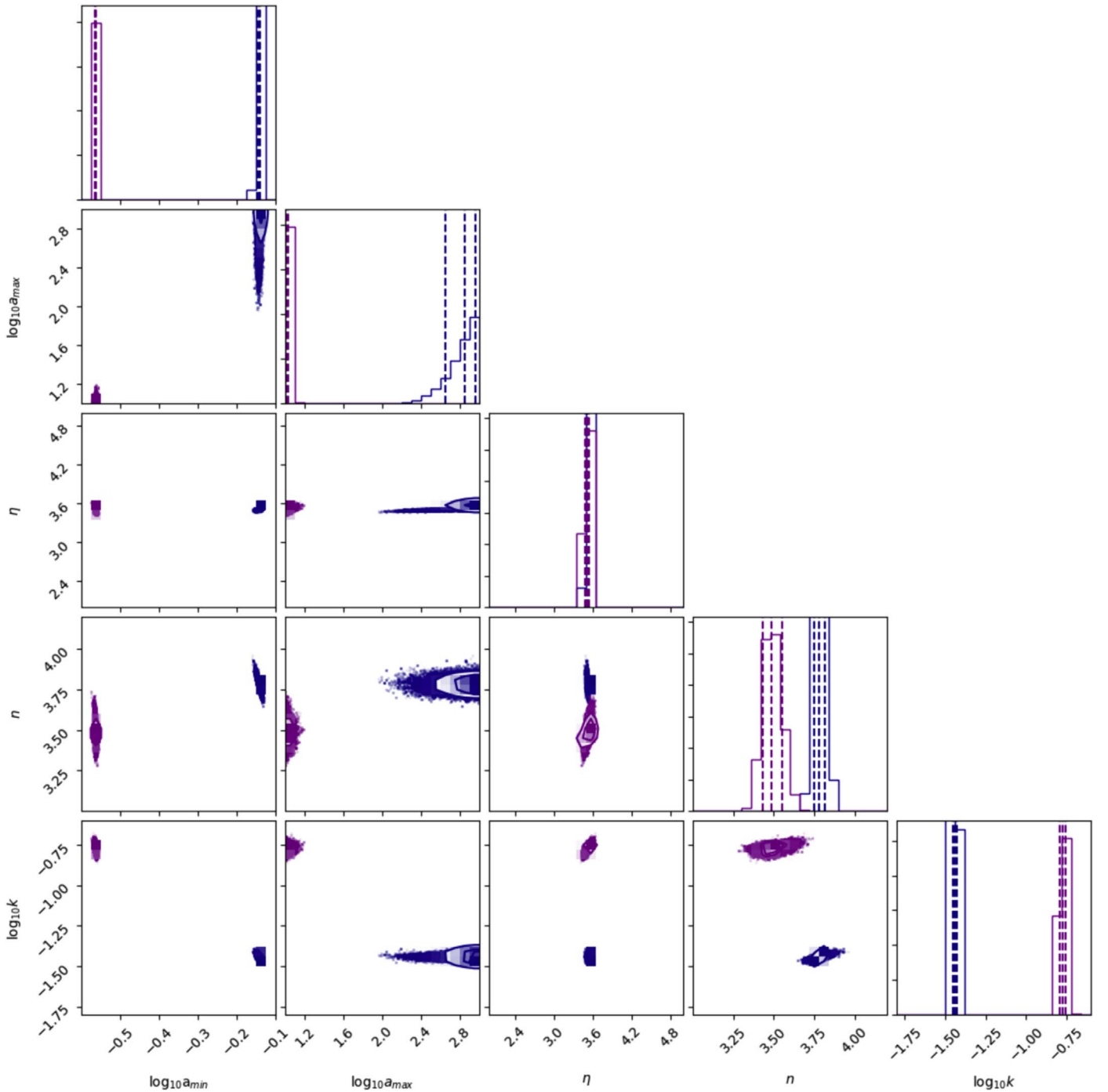


Figure 10. Posterior distributions for the joint SPF and polarizability dust properties fit. The two distinct families of acceptable models (shown in blue and purple, respectively) are considered separately in extracting the confidence intervals presented in Table 1 (as Peak 1 and 2, respectively). The vertical dashed lines mark the 16th, 50th, and 84th percentile values for each parameter and family of models.

(in particular, $a_{\max} \lesssim 11 \mu\text{m}$ at the 95% confidence level) that seems physically unlikely. In the remainder of the analysis, we focus on the first family of models.

All three fits yield consistent minimum grain sizes, $a_{\min} \approx 0.8 \mu\text{m}$. Conversely, we find that the maximum grain size is constrained to be large, with a 95% confidence level lower limit of $440 \mu\text{m}$. Finally, we note that, while the “SPF only” and “polarizability only” fits each constrain the size distribution power-law index well, they yield inconsistent

values: $\eta \approx 4.2$ and 3.5 , respectively. The “joint” fit favors the latter value, which is consistent with collisional models.

In both the “SPF only” and “polarizability only” fits, we find multimodal posteriors spanning a large fraction of the explored range for the real part of the refractive index but with little overlap between one another, indicating ambiguities in the fit. Striving to achieve a compromise between the two observed quantities, the “joint” fit has a significantly narrower posterior, $3.5 \lesssim n \lesssim 3.8$. The imaginary part of the refractive index also

Table 2
Best-fitting Geometrical Properties Based on the Stokes I Image, the Stokes Q_ϕ Image, and Both Images Simultaneously

Parameter	Prior Ranges		Best-fitting Model			Median $\pm 1\sigma$		
	Initial	Full	I	Q_ϕ	Joint	I	Q_ϕ	Joint
i ($^\circ$)	87 ± 1	[70 .. 90]	88.84	88.65	88.74	$88.88^{+0.01}_{-0.02}$	$88.59^{+0.04}_{-0.05}$	88.75 ± 0.02
h_0 (au)	5 ± 2	[0.1 .. 10]	0.10	0.10	0.10	0.13 ± 0.02	$0.102^{+0.002}_{-0.001}$	$0.11^{+0.04}_{-0.01}$
r_c (au)	100 ± 20	[50 .. 150]	99.79	95.81	98.35	$97.74^{+0.96}_{-0.79}$	$93.87^{+1.21}_{-0.90}$	$98.20^{+0.37}_{-0.56}$
r_{in} (au)	50 ± 20	[1 .. 100]	50.50	7.38	39.85	$51.8^{+2.2}_{-2.8}$	$22.2^{+7.8}_{-3.0}$	$41.8^{+2.6}_{-3.4}$
γ_1	[0 .. 5]	[0 .. 5]	4.01	3.08	3.42	$3.77^{+0.23}_{-0.20}$	$3.44^{+0.32}_{-0.31}$	$3.37^{+0.11}_{-0.12}$
γ_2	[-5 .. 0]	[-5 .. 0]	-4.79	-4.96	-4.96	$-4.60^{+0.10}_{-0.12}$	≤ -4.84	≤ -4.87
$\log_{10}(M_d(M_\odot))$	-9 ± 2	[-12 .. -4]	-7.60	-7.31	-7.57	-7.61 ± 0.01	$-7.37^{+0.01}_{-0.02}$	$-7.60^{+0.01}_{-0.02}$

Note. The full range explored for each quantity is indicated in the second column, whereas the initial range indicates the Gaussian prior that is used for most parameters.

reveals significant tension between the ‘‘SPF only’’ and ‘‘polarizability only’’ fits: the former yields an upper limit on k , $\log k \lesssim -2.8$, while the latter has a well constrained posterior, $\log k \approx -1.4 \pm 0.1$. The ‘‘joint fit’’ posterior prefers the latter solution with a secondary peak at $\log k \approx -0.8$.

We defer the interpretation of the results of our dust fitting to Section 5. For now, we note that, while the SPF and polarizability fit leave some unsolved ambiguities and tensions, the best-fitting model yields an acceptable fit to both quantities. In turn, this allows us to fix the dust properties and perform image fitting to assess the geometrical properties of the disk.

4.2. Image Modeling

4.2.1. Modeling Setup

To model the GPI total intensity and Stokes Q_ϕ images, we use the best-fitting combined dust model derived in the previous section and explore the geometrical structure of the disk. We use the MCFOST radiative transfer code (Pinte et al. 2006) to produce synthetic scattered light images. We model the debris disk density structure with the widely used functional form

$$\rho(r, z) \propto \frac{e^{-\left(\frac{|z|}{h(r)}\right)^{\gamma_{\text{vert}}}}}{\sqrt{\left(\frac{r}{r_c}\right)^{-2\gamma_1} + \left(\frac{r}{r_c}\right)^{-2\gamma_2}},$$

following Augereau et al. (1999). The critical radius, r_c , marks the transition between two power-law density regimes (with indices $\gamma_1 > 0$ and $\gamma_2 < 0$, respectively). We set $\gamma_{\text{vert}} = 2$ to yield a Gaussian vertical profile and a bow-tie shape for the disk, i.e., a constant h/r ratio. We further restrain the radial extent of the disk with inner and outer hard edges at radii r_{in} and r_{out} , mostly for computational purposes.

Given a disk geometry and a set of dust properties, MCFOST produces a full Stokes synthetic datacube with pixel scale, orientation, and field of view set to match our GPI observations. The Stokes Q and U maps are converted to a Stokes Q_ϕ image, while the star is masked out of the Stokes I image, before both are convolved by the instrumental PSF as estimated by the satellite spots. We then mask regions that are closer than the inner working angle of the Stokes I image to only consider the same pixels that were used in deriving the SPF and polarizability curve in the previous section. We also set an outer radius of $1''.6$, outside of which no trustworthy data are available. Finally, we mask out pixels that lie more than

$0''.35$ from the disk spine to ensure that the fitted region include both disk-dominated and background-dominated pixels. A likelihood is then computed using a pixel-by-pixel χ^2 calculation. Exploration of the parameter space is conducted through three independent MCMC processes—one fit for Stokes I , a second for Stokes Q_ϕ , and a third joint fit—each using three temperatures and 100 walkers. Our final results again include only the final 40%–45% of each MCMC chain, when the chains had visually achieved convergence (in total, this includes 1660, 2420, and 1380 iterations for our Stokes I fit, Stokes Q fit, and joint fit, respectively). Consistent with the dust modeling conducted above, we adopt the MI PSF-subtracted total intensity image of the disk.

In this aspect of our modeling, the geometrical free parameters are the disk inclination (i), the critical radius (r_c), the volume density power-law indices (γ_1 , γ_2), the reference scale height (h_0 , defined at $r_0 = 100$ au), and the disk inner radius (r_{in}). Given the large halo that extends well beyond the GPI field of view, we cannot constrain the disk outer radius with our data and, thus, set $r_{out} = 200$ au. Finally, we set the total disk mass (M_d) as a free parameter that defines the total amount of dust in the system, based on a representative grain density of 3.5 g cm^{-3} . So long as the disk remains optically thin, this acts as a simple multiplicative factor that serves to adjust the absolute surface brightness of the model to the observed one. We initialize γ_1 and γ_2 with uniform distributions, and all other free parameters are assigned a Gaussian prior, either based on our empirical geometrical analysis (i , r_c , h_0 , from Section 3.3) or assuming a conservatively broad range (r_{in} , M_d). The explored ranges for each parameter are indicated in Table 2.

4.2.2. Results

The results of our MCMC chain are summarized in Table 2. Figure 11 displays the full posterior distribution for all parameters in the combined fit, and Figure 12 shows the model images for the overall best-fitting model. While the posteriors appear multimodal, particularly for H_0 , we inspected the movement of the walkers in the MCMC chains to confirm that the chains had been decoupled from their initial state. The results of fitting separately the Stokes I and Q_ϕ images are mostly similar to those of the joint fit; however, the scatter in some of the parameter values exceeds the nominal uncertainties from the MCMC chains. For instance, fitting the polarized intensity image yields a 10% smaller disk radius and a $0^\circ 2$

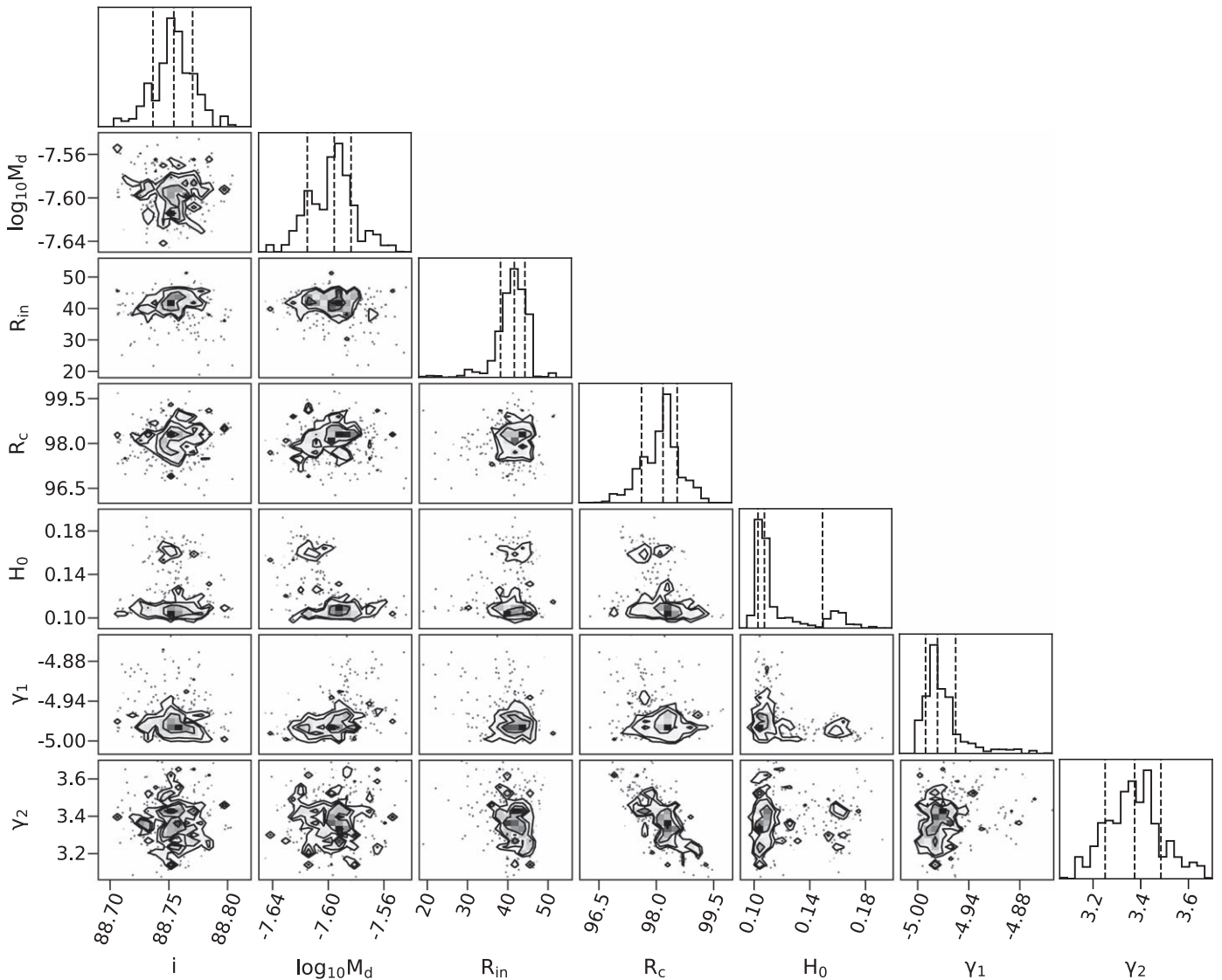


Figure 11. Posterior probability distribution for all free parameters in the joint fit to Stokes I and Q_ϕ intensity images.

lower inclination. In the following, we consider all three separate fits holistically in our analysis.

Overall, the best-fitting model reproduces well the observed images, at least within the region used in the likelihood function. However, given the high signal-to-noise of our data set, the residuals are statistically significant, indicating that the model has some shortcomings. In particular, both the Stokes I and Q_ϕ residual maps reveal a thin trace along the disk spine, suggesting that the model is slightly too extended vertically. Since we have allowed the vertical thickness of the disk to be very small (h/r as low as 0.1%), it is possible that this is due to our use of a slightly too broad instrumental PSF. We also find systematic residuals in the Stokes Q_ϕ image at the location of the ring ansae. This may be a consequence of imperfection in the dust scattering properties as derived in the previous section. Furthermore, we also note that the best-fitting model underpredicts the polarized intensity in the immediate vicinity of the inner working angle of that image, a region not included in the fit. Finally, there are marginally significant positive residuals in the total intensity image outside of the ring radius. This is likely due to the lack of treatment of the halo in our model; however, we stress that only the region within the ring radius is strongly

detected in our data. Altogether, in spite of these limitations, we consider that the quality of the fit is sufficient to warrant a discussion of the main results from our exploration of the parameter space.

All geometric parameters are well constrained in the fit, except for r_{in} as a consequence of the steep inner surface density profile. Considering first the joint fit (to the Stokes I and Q_ϕ images simultaneously), we derive an inclination of $i \approx 88.7^\circ \pm 0.1^\circ$, which is about 0.5° higher than the best-fit value obtained in the geometrical analysis in Section 3.3. This is an indication that either our model is imperfect, or some of the assumptions that we used in empirically deriving the ring geometry are incorrect. This is further supported by the fact that we find a rather broad ring, with an inner radius 2–4 times smaller than $r_c \approx 100$ au. Nonetheless, the latter is consistent with the ring radius we had derived in Section 3.3. Although dust extends over a broad range of stellocentric distances, the power-law volume density profiles are relatively steep ($\gamma_1 \approx 3.5$ and $\gamma_2 \lesssim -4.5$). The surface density profile is characterized by an FWHM of about 40 au. This $\approx 40\%$ radial width is uncomfortably high to fully validate the narrow ring approximation of our initial geometric fitting and derivation of

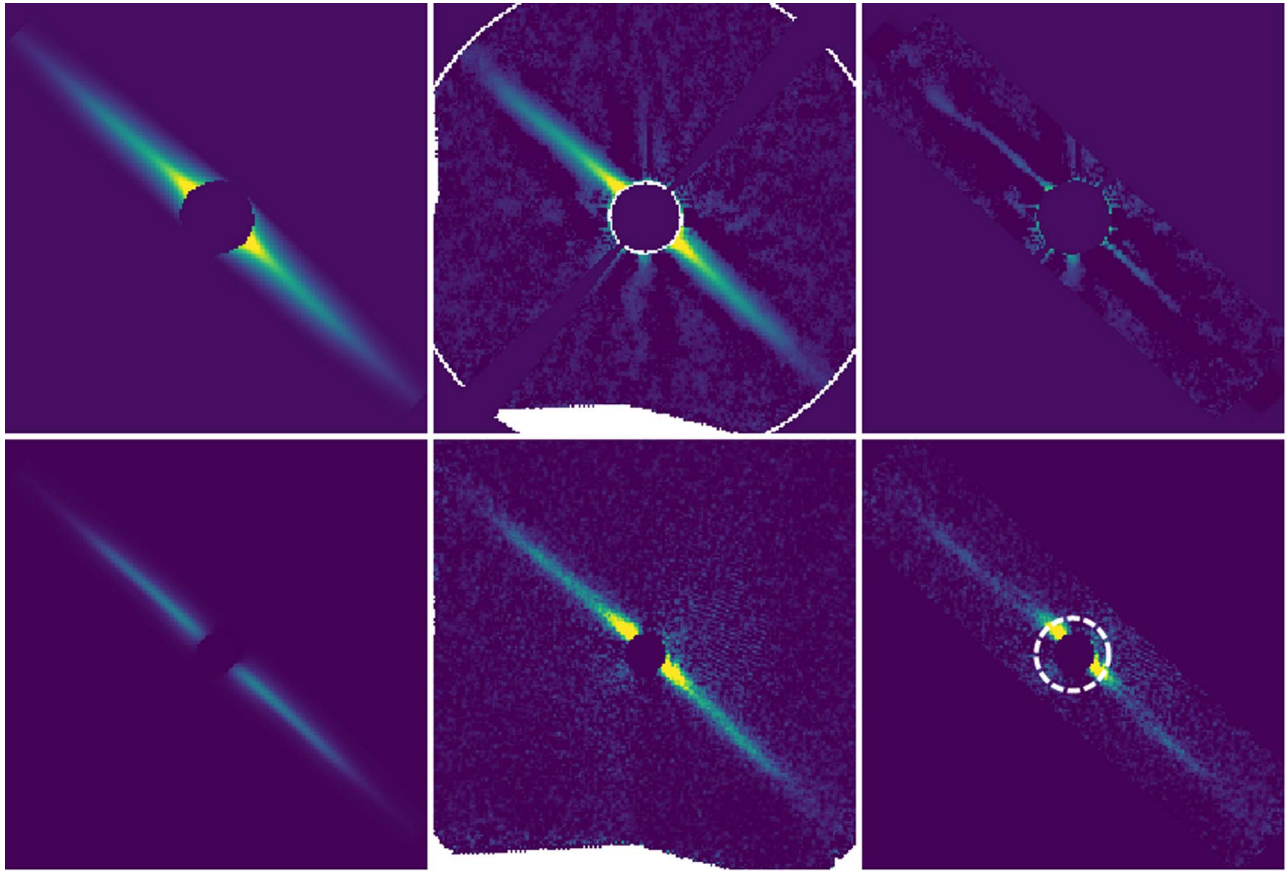


Figure 12. Best-fitting total and polarized intensity images for HD 32297 (top and bottom rows, respectively). From left to right in each row is the model image, H -band data image, and residuals all on the same scaling (square root stretch for Stokes I , linear stretch for Stokes Q_ϕ). In the bottom right panel, the dashed circle indicates the inner working angle used in estimating the SPF and polarizability curve. Data inside of that circle are not included in the dust property fit and, consequently, are not included in the image fit either to prevent any bias. The residuals are shown here for visual display only.

the SPF and polarizability curves. Nonetheless, the effect of this width is to blur the location of the ring spine and the dependencies on scattering angle, not to systematically bias these. We therefore expect our prior estimates to be representative of the true quantities, which is supported by the good match in the mean ring radius, for instance.

The surprisingly small disk scale height ($h/r \approx 0.2\%$) appears to contradict our finding that the disk is marginally resolved along the vertical direction (see Section 3.3). Aside from the possibility that the PSF we used in the image modeling may not be a perfect match to the HD 32297 data set, this may be an indication that the vertical density distribution is not Gaussian. If the profile is more condensed in the center, e.g., following a Lorentzian or exponential profile, the assumption of a Gaussian profile in both our initial geometrical analysis and in radiative transfer modeling would overestimate slightly the vertical extent of the disk. Finally, the PSF subtraction process could have slightly attenuated the lower surface brightness regions away from the midplane in the total intensity image, thus leading to a similar effect. The fact that the fit to the polarized intensity image also favors a very small disk thickness rather points to other explanations, however.

Finally, the total dust mass, $M_d \approx 0.01M_\oplus$, should be considered with caution, as this quantity is strongly correlated with dust properties, particularly the minimum grain size and porosity. Since we have not attempted to fit for an actual composition, the true mean grain density is not a parameter of our model and is degenerate with the total mass. It is

nonetheless interesting to note that this is much smaller than the dust mass derived from the millimeter emission of the system ($\approx 0.6M_\oplus$; MacGregor et al. 2018).

5. Discussion

5.1. System Geometry

The combination of high angular resolution and exquisite image fidelity enabled by GPI offers an opportunity to determine the ring geometry in a precise manner. This is further enhanced by the fact that the polarized intensity image does not require any PSF subtraction. It is thus interesting to note that the disk radius that we determined here, both from the direct geometric analysis and from the direct image fitting (Sections 3.3 and 4.2, respectively), is markedly smaller than has been found in past studies: around 100 au compared to 130 au. We emphasize that this difference is not a result of the updated distance to the system, as we have already accounted for it. In other words, the angular radius of the ring we find is about 40% smaller than those reported in previous studies. Notably, the two methods we employed rely on very different aspects of the data. Image fitting is inherently weighted by the signal-to-noise and, thus, by the local brightness of the disk, which places a different emphasis on different regions of the disk. The geometric approach, instead, is mostly independent of the surface brightness profile. Arguably, the latter is a more robust approach to determining the disk geometry. In particular, self- and over-subtraction effects have a much more

direct influence on the surface brightness distribution, and inadequately taking them into account is more likely to introduce biases than focusing on the spine of a nearly edge-on disk like HD 32297. The latter is now precisely traced as close as $0''.12$ from the star (this study; see also Bhowmik et al. 2019), and the remaining dominant source of uncertainty may actually be the location of the star itself. In particular, Bhowmik et al. (2019), who derived a disk radius from their SPHERE images that is consistent with past studies, suggest an offset of $\approx 0''.01$ of the star in the direction perpendicular to the disk, whereas our analysis reveals no such offset. While the nominal precision in the position of the star with instruments such as GPI and SPHERE is significantly better, this suggests that systematic uncertainties are not fully understood in these complex instruments.

Despite these systematic errors associated with scattered light images, the submillimeter emission of the system supports an 80–120 au radial range for the ring (MacGregor et al. 2018). Even though the inferred surface density profile rises as roughly r^2 in their best-fitting model, the r^{-2} illumination dependency of impinging starlight yields a flat surface brightness profile and, thus, a roughly 100 au radius for the scattered light ring. Similarly, the mid-infrared emission from the system suggests an inner disk radius of about 80–90 au (Fitzgerald et al. 2007; Moerchen et al. 2007). While the scattered light images of the system may probe physically distinct grains (and there is evidence for millimeter-emitting dust in the halo surrounding the parent body belt; MacGregor et al. 2018), it seems implausible that the scatterers would be located exclusively outside of the parent body belt. This is definitely not the case in the well-studied, lower inclination, HR 4796 system (Kennedy et al. 2018). We therefore conclude that the HD 32297 ring is indeed centered at about 100 au, as inferred from the modeling of our near-infrared image.

Outside of the parent body ring, the HD 32297 system is characterized by a large-scale halo structure that lies mostly outside of our field of view. Consistent with past imaging, our observations confirm that the disk extends radially beyond the ring ansae, smoothly connecting the parent body ring and the outer halo. This confirms that the dust located in the halo most likely represents small dust grains that originated in the parent body belt before being radiatively pushed on high-eccentricity orbits, where another mechanism then sweeps them out in the NW direction. The fact that the halo is undetected to the NW of the star in our total intensity image, despite this region being the brightest of the halo (e.g., Schneider et al. 2014), could simply be due to the use of PSF subtraction techniques that effectively cancel out extended, low-gradient surface density structures. On the other hand, our polarized intensity image is free of such an effect and, yet, we find no evidence of the presence of the halo. To assess the meaningfulness of this non-detection, we compare our Q_ϕ image with the Hubble Space Telescope (HST)/STIS broadband image from Schneider et al. (2014) in the following manner: we compute surface brightness profiles in $0''.15$ bands orthogonal to the disk midplane and located $0''.75$ on either side of the star, i.e., roughly at the disk ansae. Both profiles are averaged to improve signal-to-noise given the lack of marked asymmetry in the halo within the central arcsec. We further rebin the GPI data to roughly match the $0''.05$ pixel scale of the STIS image. The resulting surface brightness profiles are shown in Figure 13. The swept-back halo is clearly visible in the STIS surface bright profile, most

prominently as an extended structure to the NW of the disk, but it is absent in the GPI polarized intensity image with a high degree of significance. Besides the NW extension of the profile, we also find the GPI surface brightness profile to be much narrower around the disk spine than the STIS one. This indicates that the halo also extends radially in front of the parent body ring.

There are two main possible explanations for the lack of detection of the halo in the STIS Q_ϕ image despite the high signal-to-noise detection of the ring itself: either the halo is much bluer than the main ring, or it is characterized by a significantly lower polarization fraction. The latter is inconsistent with the observations that the polarization fraction keeps rising outside of the parent body ring (Figure 7). On the other hand, the large-scale structure of the system has long been known to be much bluer than the star itself (Kalas 2005), whereas the main ring itself is neutral or slightly red (e.g., Esposito et al. 2014; Rodigas et al. 2014). We therefore believe that the blue color of the halo is primarily responsible for the lack of detection in our data set. Additionally, we note that the halo is also not apparent to the NW of the star in the J -band Q_ϕ SPHERE image of the system (Bhowmik et al. 2019). Overall, the only evidence for the halo in near-infrared images of the system is the curved extension of the disk midplane beyond the ansae due to limb brightening.

5.2. Scattering Properties

One of the motivations to obtain high-fidelity scattered light images of debris disks is to constrain the properties of the dust grains they contain. The surface brightness and color of debris disks are the primary observables affected by dust composition in scattered light images. In addition, polarization measurements provide further information regarding the porosity of grains, since, all else equal, large, porous grains have similar properties to smaller, compact grains (Graham et al. 2007; Shen et al. 2009). Assuming that Mie theory accurately describes the scattering properties of dust grains, the minimum grain size and the power-law index for the grain size distribution should be tightly constrained by measurements of the scattering phase function and polarization fraction. Indeed, our modeling successfully reproduced both the SPF and the polarizability curve observed for HD 32297. The size distribution inferred from our modeling, with a minimum grain size of $\approx 1 \mu\text{m}$ that is commensurable with the blowout size and a slope consistent with collisional cascade models, is in good agreement both with past studies of the system (including through thermal emission; see for instance Donaldson et al. 2013) and with general theoretical expectations.

Despite these apparent successes, it is important to emphasize that the refractive index derived from our analysis lies in a region of the parameter space that is far from all standard dust species, as illustrated in Figure 14. Worse still, no combination of such species (including void to represent porosity) is consistent with the inferred refractive index. This casts serious doubt on the physical meaning of the other dust parameters that were considered in this analysis. In other words, while we did find a combination of parameters that well reproduces the observed SPF and polarizability curve, it may be the case that this is only a practical empirical model but not one to be trusted at the physical level. There is increasing evidence that dust grains in both the solar system and in debris disks are aggregates of smaller, sub-micron monomers (e.g.,

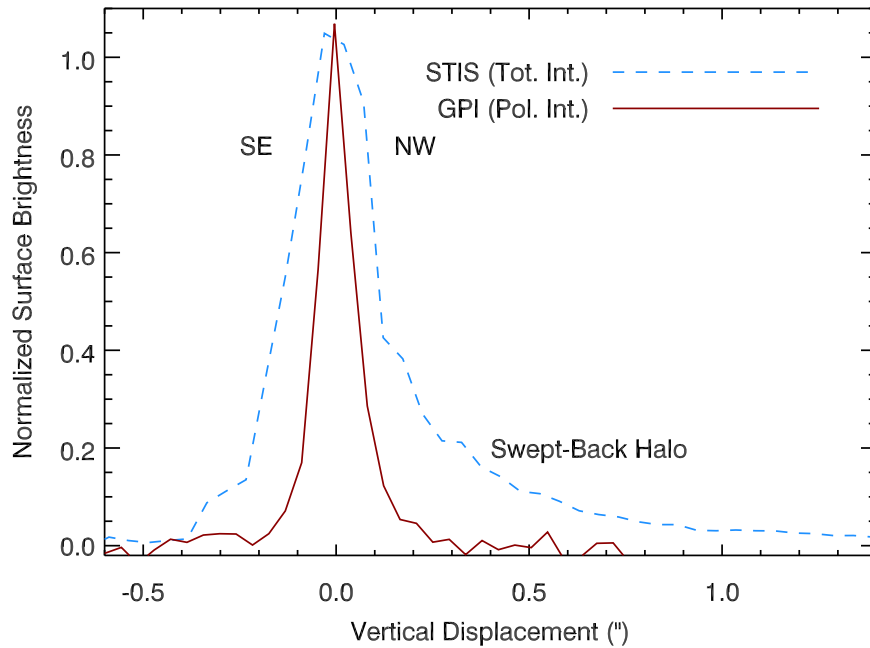


Figure 13. Surface brightness profile measured perpendicular to the disk midplane at a distance of $0.75''$ from the central star (the two sides are averaged). The dashed blue and solid red curves represent the HST/STIS total optical intensity and the GPI H -band Q_ϕ images, respectively.

Bentley et al. 2016), in which case the Mie model is irrelevant. Unfortunately, despite significant strides toward characterizing the scattering properties of aggregates, it remains beyond the reach of current models to consider aggregates whose sizes exceed the blowout size by one or more order of magnitude (Arnold et al. 2019), which we know are present in debris disks. Furthermore, it may also be instructive to revisit the assumption that the grain size distribution follows a simple power law. Collisional models suggest a more complex underlying structure when factoring in the effects of stellar gravity and radiation pressure in addition to the collisional cascade replenishing the disk (e.g., Krivov et al. 2006; Thebault et al. 2014).

Leaving aside the physical interpretation of the SPF and polarizability curves, our data provide a robust empirical characterization of the scattering properties of the HD 32297 dust ring. With the number of debris disks with estimated SPFs and/or polarizability curves slowly rising, it is now possible to perform model-independent comparisons between systems to identify commonalities and differences between systems. Hughes et al. (2018) pointed out that most solar system dust populations share a similar SPF and that the few debris disks with estimated SPFs also match that template. The SPF we have derived for HD 32297 is also in reasonable agreement with that “generic” SPF. On the other hand, the SPF determined by Milli et al. (2017) for the HR 4796 ring is markedly different. Combined with the unusual polarization fraction curve observed in that system (Perrin et al. 2015), this suggests that this latter disk is characterized by a markedly different dust population. While such comparisons are best performed by extracting the SPF from observations, this process suffers from possible ambiguities and possible biases, as we have already discussed.

To illustrate the effects of a different SPF on the appearance of a debris disk, we compared the modeled surface brightness profile along the spine of a nearly edge-on disk (using the geometric parameters indicated in Table 2) assuming three

distinct SPFs: the best-fitting Mie model presented in Section 4.1, the “generic” SPF from Hughes et al. (2018), and the HR 4796 SPF from Milli et al. (2017). The latter SPF is not defined at all scattering angles due to our particular viewing geometry of the system, so we performed linear extrapolations of the SPF for scattering angles $<15^\circ$ and $>165^\circ$. These regions are behind the coronagraphic mask once the disk is observed with the viewing geometry of HD 32297; therefore, the details of this extrapolation are not critical to the comparison. The results of this exercise are illustrated in Figure 15. All three models under-predict the surface brightness profile outside of the main ring radius, but both the best Mie model and the generic SPF match the data extremely well inside of that projected distance. This confirms that the total intensity scattering properties of the HD 32297 dust are consistent with most other astrophysical dust populations. Conversely, if this disk was characterized by an SPF that is similar to that observed for HR 4796, its surface brightness profile would be dramatically different, with a nearly flat surface brightness profile that is inconsistent with the observations. This is due to the combination of (1) the fact that the HR 4796 SPF has its minimum at a scattering angle of $\approx 50^\circ$ with significant backscattering at angles $\gtrsim 100^\circ$, and (2) limb brightening in the optically thin ring. This is further evidence that the scattering properties in the HD 32297 and HR 4796 debris disks are clearly distinct.

An additional qualitative feature of the SPF in HD 32297 is the sharp peak observed in polarized intensity close to the inner working angle of our observations. Since the polarization fraction is expected by symmetry to drop to zero at 0° scattering angle, this indicates the SPF itself must be characterized by a very sharp forward scattering peak, reminiscent of those of HR 4796 and β Pic (Millar-Blanchaer et al. 2015; Perrin et al. 2015; P. Arriaga et al. 2020, in preparation). On the other hand, there are several edge-on debris disks that have been imaged in polarized intensity that do not show such a feature (Olofsson et al. 2016; Engler et al. 2017; Esposito et al. 2018, 2020, submitted). This further hints at

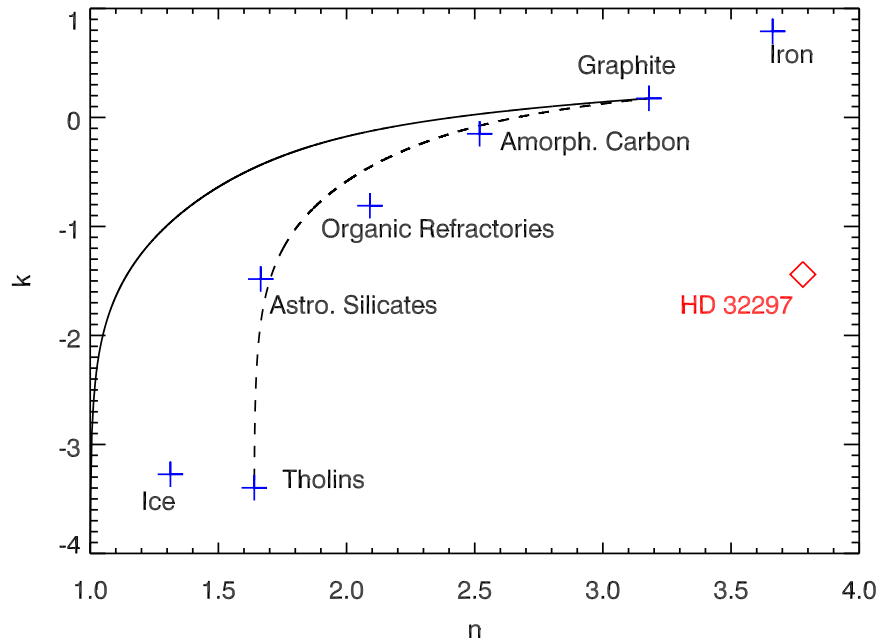


Figure 14. Real and imaginary refractive indices at $1.65 \mu\text{m}$ of standard dust species (blue crosses, Draine & Lee 1984; Khare et al. 1984; Draine 1985; Pollack et al. 1994; Zubko et al. 1996; Li & Greenberg 1997, 1998) and of our best-fitting model to the HD 32297 SPF and polarizability curve (red diamond). The solid and dashed curves illustrate the effect of porosity and mixed composition, respectively, using the Bruggeman rule of effective medium theory.

the fact that the scattering properties of dust populations in debris disks are not all identical; however, interpreting them in terms of physical properties of the grains may still be out of reach.

Finally, another qualitative approach to constraining the SPF in the case of nearly edge-on disks like HD 32297 is to assess whether the back side of the ring contributes to the scattered light image. Bhowmik et al. (2019) presented a tentative detection in total intensity using ADI PSF subtraction, which would imply a strong backscattering peak. We do not confirm this feature in our observations of HD 32297. It is possible that differences between PSF subtraction introduce different artifacts, precluding a definitive conclusion. However, we point out that, given the derived disk radius and inclination, the projected separation along the minor axis between the front and back side of the ring is in the $0''.04\text{--}0''.07$ range, which makes it extremely challenging to detect. In polarized intensity, which is unaffected by PSF subtraction, the lack of an increase in vertical extent of the disk just inside of the ansae indicates that the back side of the ring does not contribute significantly to the observed surface brightness, indicating that the SPF drops significantly around a scattering angle of 90° . This latter conclusion matches our conclusion that the SPF of HD 32297 is qualitatively different from that observed in HR 4796.

5.3. Underlying Planetary System

Debris disks are believed to be associated with planetary-mass objects, as readily illustrated in some well-known systems, such as β Pic and HR 8799. No point source is evident in our total intensity image of the system. We note, however, that observations with GPI’s polarization mode are not optimal for detection of planets unless they are highly linearly polarized. Instead, integral field spectroscopy observations provide the deepest search for planets. Bhowmik et al. (2019) presented such observations of HD 32297, reaching a contrast limit of 10^{-5} or better outside of $0''.5$. At an assumed

age of 30 Myr, this corresponds to an upper limit on any planetary-mass object of $4\text{--}5 M_{\text{Jup}}$ based on the COND models (Baraffe et al. 2003). An important caveat, however, is that the detection limit is much worse along the bright disk spine, so that the upper limit computed only applies outside of the plane of the disk. Specifically, a 10^{-5} contrast point source would have its peak pixel brightness equal to that of the disk and, therefore, would be marginally detectable at best, at a distance of $\approx 1''.2$ from the star if it lies in the plane of the disk. At closer separation, the contrast degrades proportionally to the disk peak surface brightness, reaching 10^{-4} (or a planet mass of $\approx 12 M_{\text{Jup}}$) at $\approx 0''.45$.

An indirect probe of the presence of planetary-mass bodies in the system is through their dynamical interaction with the disk. The lack of significant lateral asymmetry and of local (photometric or morphological) perturbation in the parent body belt supports the picture of a dynamically cold, azimuthally symmetric system, seemingly ruling out strong planet–disk interactions. The scale height of the belt can be also related to its dynamical excitation, since the scale height is directly related to the velocity dispersion of the solid bodies. The disk scale height derived from our geometric analysis ($h/r \approx 0.04$) is consistent with dynamical models that only consider collisions between grains and radiative forces (Thebault 2009). Therefore, the dynamical state of the HD 32297 main belt can be fully explained without invoking the presence of planetary-mass bodies stirring the system. A planet could, however, be responsible for the inner dust depletion (inside of $30\text{--}50$ au) without introducing measurable local perturbation. In addition, Lee & Chiang (2016) proposed that an interior planet on an inclined orbit is responsible for the “double wing” in the extended outer halo (Schneider et al. 2014); however, this could also arise from interaction with secondary gas (Lin & Chiang 2019). Current observations of the HD 32297 system are thus inconclusive regarding the presence and structure of its planetary system.

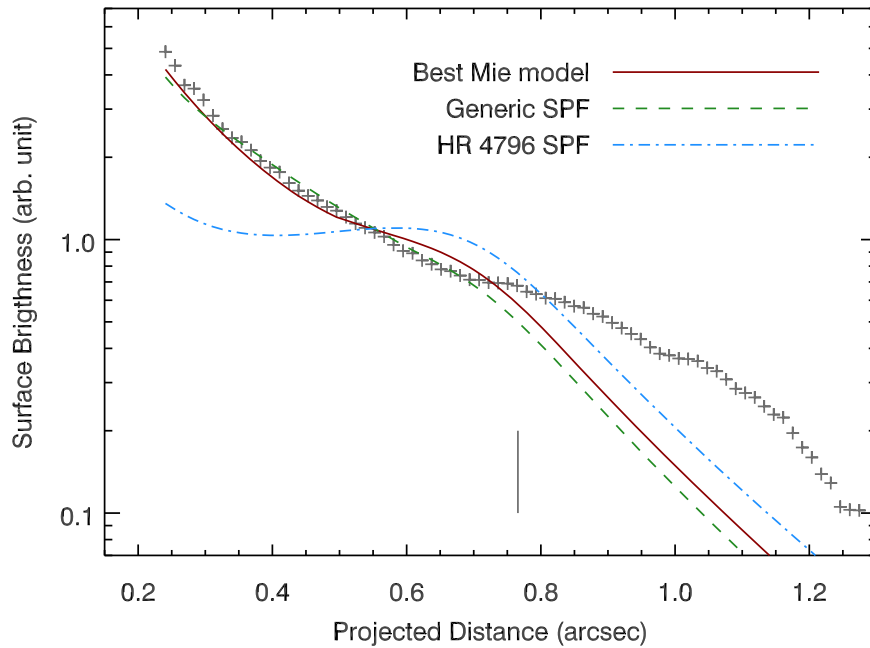


Figure 15. Observed H -band total intensity surface brightness profile for HD 32297 (gray plus signs) compared to predicted profiles assuming different SPFs. The solid red, dashed green, and blue dotted–dashed curves correspond to the best-fitting Mie model derived in this study, the generic SPF identified by Hughes et al. (2018), and the HR 4796 SPF from Milli et al. (2017), respectively. The vertical segment marks the location of the ring radius, as inferred from our geometric analysis (Section 3.3).

6. Conclusion

As part of the commissioning phase of the GPI instrument, we have obtained H -band high-contrast total and polarized intensity images of the edge-on HD 32297 debris disk. The disk is detected from just outside the edge of the coronagraphic mask, $\approx 0''.15$ from the central star, out to edge of the field of view, at a projected distance of $\approx 1''.3$. Using the slight curvature of the disk spine, we determined the disk geometry and found that the disk radius is ≈ 100 au, smaller than previous scattered light studies of the system, highlighting the difficulty of measuring disk size in an edge-on configuration. However, since the radius we derive is consistent with the thermal emission images of the disk, we believe that it represents the true size of the parent body belt.

We applied four multiple PSF subtraction post-processing algorithms and demonstrated that three of these methods yield reliable surface brightness distributions in the case of an edge-on disk. Using these, we found that the disk is consistent with being azimuthally symmetric. We also estimated the SPF and polarizability curves of the dust present in the disk. We find curves that are typical of solar system dust populations and of other debris disks, with the marked exception of the HR 4796 debris disk. Assuming Mie scattering, we find a dust model that simultaneously reproduces the SPF and polarizability curves, but the resulting refractive index is inconsistent with any standard dust composition. The most likely explanation is that dust grains in the system are not compact spheres but complex aggregates, as seen in solar system dust populations.

The large-scale swept-back halo present outside of the parent body ring is undetected in our data, confirming that it contains primarily sub-micron grains that produce blue scattering. Finally, we do not detect any planetary-mass object in the system, although we stress that our detection limit is severely limited by the bright disk for objects whose orbits are coplanar with the disk itself. Given the symmetric and small vertical

extent of the parent body belt, we find no evidence for stirring induced by an unseen planetary-mass body; however, we cannot exclude the presence of an object that is sufficiently distant from the belt.

We are grateful to Glenn Schneider for making his STIS image available for analysis. This work is based on observations obtained at the Gemini Observatory, which is operated by the Association of Universities for Research in Astronomy, Inc. (AURA), under a cooperative agreement with the National Science Foundation (NSF) on behalf of the Gemini partnership: the NSF (United States), the National Research Council (Canada), CONICYT (Chile), Ministerio de Ciencia, Tecnología e Innovación Productiva (Argentina), and Ministério da Ciência, Tecnologia e Inovação (Brazil). This work made use of data from the European Space Agency mission Gaia (<https://www.cosmos.esa.int/gaia>), processed by the Gaia Data Processing and Analysis Consortium (DPAC, <https://www.cosmos.esa.int/web/gaia/dpac/consortium>). Funding for the DPAC has been provided by national institutions, in particular, the institutions participating in the Gaia Multilateral Agreement. This research made use of the SIMBAD and VizieR databases, operated at CDS, Strasbourg, France.

This work was supported by NSF grants AST-1411868 (E.L.N., K.B.F., B.M., and J.P.), AST-141378 (G.D.), and AST-1518332 (T.M.E., R.J.D.R., J.R.G., P.K., and G.D.). This work was also supported by NASA grants NNX14AJ80G (E.L.N., B.M., F.M., and M.P.), NNX15AC89G and NNX15AD95G/NESS (T.M.E., B.M., R.J.D.R., G.D., J.J.W., J.R.G., and P.K.), NN15AB521 (D.S.). M.R. is supported by the NSF Graduate Research Fellowship Program under grant No. DGE-1752134. J.R. and R.D. acknowledge support from the Fonds de Recherche du Québec. J.M.’s work was performed in part under contract with the California Institute of Technology/Jet Propulsion Laboratory funded by NASA through the Sagan Fellowship Program executed by the NASA Exoplanet Science

Institute. M.M.B. and J.M. were supported by NASA through Hubble Fellowship grants #51378.01-A and HST-HF2-51414.001, respectively, and I.C. through Hubble Fellowship grant HST-HF2-51405.001-A, awarded by the Space Telescope Science Institute, which is operated by AURA, for NASA, under contract NASS-26555. J.J.W. is supported by the Heising-Simons Foundation 51 Pegasi b postdoctoral fellowship. This work benefited from NASA’s Nexus for Exoplanet System Science (NExSS) research coordination network sponsored by NASA’s Science Mission Directorate. Portions of this work were also performed under the auspices of the U.S. Department of Energy by Lawrence Livermore National Laboratory under Contract DE-AC52-07NA27344.

Facility: Gemini:South.

Software: MCFOST (Pinte et al. 2006), Gemini Planet Imager Data Reduction Pipeline (Perrin et al. 2014, 2016, <http://ascl.net/1411.018>), pyKLIP (Wang et al. 2015, <http://ascl.net/1506.001>), NumPy (Oliphant 2006, <https://numpy.org>), SciPy (Jones et al. 2001, <http://www.scipy.org/>), Astropy (The Astropy Collaboration et al. 2018), matplotlib (Hunter 2007; Droettboom et al. 2017), iPython (Pérez & Granger 2007), emcee (Foreman-Mackey et al. 2013, <http://ascl.net/1303.002>), corner (Foreman-Mackey 2016, <http://ascl.net/1702.002>).

Appendix

Surface Brightness Preservation of PSF Subtraction Methods: Injection-and-recovery Test

The various PSF subtraction methods we employed suffer from several potential limitations: self- and over-subtraction, significant correlated residuals, poor sensitivity to smooth, and extended surface brightness such as the HD 32297 halo, to name the most important ones. Besides assessing the geometry of the disk, our goal is to measure the surface brightness profile of the disk, which requires understanding the amplitude of these effects. Forward modeling, which maps out the throughput of PSF subtraction

methods, is necessary when applying the standard ADI method (e.g., Boccaletti et al. 2012; Esposito et al. 2014, in the case of HD 32297), but ultimately, the precision of the process is limited by the fact that (1) the self- and/or over-subtraction is a large fraction of the input surface brightness, and (2) a bright disk like in the case of HD 32297 results in a breakdown of the assumption that the astrophysical signal is small compared to the stellar PSF brightness.

To circumvent the limitations of ADI, we used the RDI, MI, and NMF methods, which we expect to result in small (or negligible) surface brightness loss, at least along the disk spine. To assess the reliability of these methods, we perform an injection-and-recovery test. Out of all of the reference frames used in the RDI subtraction, we identified the HIP 46634 data set (taken on 2015 February 1) as the most correlated with the HD 32297 one. Visual inspection confirmed the clear similarities in the PSF structure between both data sets. We generated a synthetic disk model. For simplicity, we assumed the disk to be exactly edge-on, assumed a surface brightness profile that obeys an $r^{-1.5}$ power law, and assumed a vertical structure characterized by a ≈ 2 pixel FWHM Gaussian profile. Those choices were made to roughly match the appearance of the HD 32297 disk. The disk model image was then convolved by a 4 pixel FWHM two-dimensional Gaussian appropriate for GPI in the H band, and the disk surface brightness was scaled relative to the input data set to match the observed disk. In particular, since HIP 46634 is about 0.8 mag brighter in the H band than HD 32297, the surface brightness of the injected model is higher than that of the HD 32297 disk. We then injected this disk in each individual frame of HIP 46634 and performed the same PSF subtraction process as described above. We did not use ADI in this test, as it has already been established that this method does not preserve the flux of extended disks (Esposito et al. 2014, in the case of HD 32297).

Figure A1 shows the resulting inferred surface brightness profiles compared to the input model. The RDI, MI, and NMF

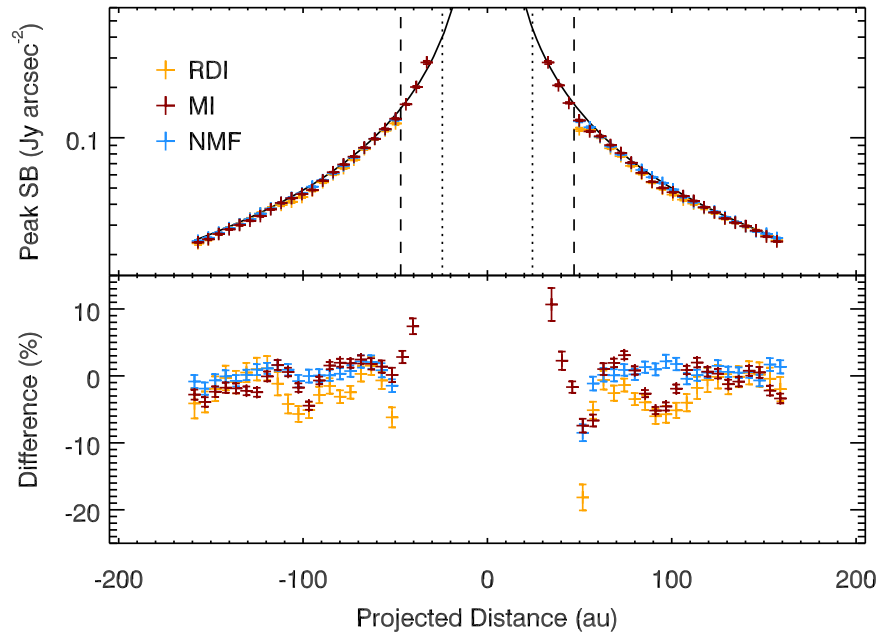





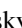






Figure A1. Top panel: input (solid black curve) and retrieved peak surface brightness of a model edge-on disk injected in a disk-free GPI data set. The results from three PSF subtraction methods are shown here: RDI, MI, and NMF (orange, red, and blue symbols, respectively). The vertical dotted (dashed) lines indicate the smallest separations at which the MI- (RDI- or NMF-) processed image can be trusted. Bottom panel: relative difference between the input and output surface brightness profiles.

methods retrieve the full surface brightness of the disk's spine to within 10%, albeit with some radial substructures. We stress that the degree of reliability may depend on the specific data set used in the injection. Nonetheless, it is encouraging that peak surface brightness is preserved to such high precision by the different methods we employed. On the other hand, measuring integrated brightness in vertically extended boxes centered on the disk results in larger discrepancies (up to $\approx 30\%$), as the PSF subtraction process tends to remove some signals in the lower surface brightness regions away from the disk spine. Despite these imperfections, this analysis confirms that all three non-ADI PSF subtraction methods preserve the total intensity profile of the disk along its spine.

ORCID iDs

Gaspard Duchêne  <https://orcid.org/0000-0002-5092-6464>
 Malena Rice  <https://orcid.org/0000-0002-7670-670X>
 Justin Hom  <https://orcid.org/0000-0001-9994-2142>
 Joseph Zalesky  <https://orcid.org/0000-0001-9828-1848>
 Thomas M. Esposito  <https://orcid.org/0000-0002-0792-3719>
 Maxwell A. Millar-Blanchaer  <https://orcid.org/0000-0001-6205-9233>
 Bin Ren  <https://orcid.org/0000-0003-1698-9696>
 Paul Kalas  <https://orcid.org/0000-0002-6221-5360>
 Michael P. Fitzgerald  <https://orcid.org/0000-0002-0176-8973>
 Pauline Arriaga  <https://orcid.org/0000-0001-6364-2834>
 Joanna Bulger  <https://orcid.org/0000-0003-4641-2003>
 Christine H. Chen  <https://orcid.org/0000-0002-8382-0447>
 Eugene Chiang  <https://orcid.org/0000-0002-6246-2310>
 Tara Cotten  <https://orcid.org/0000-0003-0156-3019>
 Ian Czekala  <https://orcid.org/0000-0002-1483-8811>
 Robert J. De Rosa  <https://orcid.org/0000-0002-4918-0247>
 Ruobing Dong  <https://orcid.org/0000-0001-9290-7846>
 Zachary H. Draper  <https://orcid.org/0000-0002-1834-3496>
 Katherine B. Follette  <https://orcid.org/0000-0002-7821-0695>
 Li-Wei Hung  <https://orcid.org/0000-0003-1498-6088>
 Bruce Macintosh  <https://orcid.org/0000-0003-1212-7538>
 Johan Mazoyer  <https://orcid.org/0000-0002-9133-3091>
 Stan Metchev  <https://orcid.org/0000-0003-3050-8203>
 Marshall D. Perrin  <https://orcid.org/0000-0002-3191-8151>
 Julien Rameau  <https://orcid.org/0000-0003-0029-0258>
 Inseok Song  <https://orcid.org/0000-0002-5815-7372>
 Jason Wang  <https://orcid.org/0000-0003-0774-6502>
 Schuyler Wolff  <https://orcid.org/0000-0002-9977-8255>
 Ben Zuckerman  <https://orcid.org/0000-0001-6809-3045>
 S. Mark Ammons  <https://orcid.org/0000-0001-5172-7902>
 Vanessa P. Bailey  <https://orcid.org/0000-0002-5407-2806>
 Travis Barman  <https://orcid.org/0000-0002-7129-3002>
 Jeffrey Chilcote  <https://orcid.org/0000-0001-6305-7272>
 Benjamin L. Gerard  <https://orcid.org/0000-0003-3978-9195>
 Stephen J. Goodsell  <https://orcid.org/0000-0002-4144-5116>
 Alexandra Z. Greenbaum  <https://orcid.org/0000-0002-7162-8036>
 Pascale Hibon  <https://orcid.org/0000-0003-3726-5494>
 Patrick Ingraham  <https://orcid.org/0000-0003-3715-8138>
 Quinn Konopacky  <https://orcid.org/0000-0002-9936-6285>
 Franck Marchis  <https://orcid.org/0000-0001-7016-7277>
 Mark S. Marley  <https://orcid.org/0000-0002-5251-2943>
 Christian Marois  <https://orcid.org/0000-0002-4164-4182>

Eric L. Nielsen  <https://orcid.org/0000-0001-6975-9056>
 Rebecca Oppenheimer  <https://orcid.org/0000-0001-7130-7681>
 Abhijith Rajan  <https://orcid.org/0000-0002-9246-5467>
 Fredrik T. Rantakyro  <https://orcid.org/0000-0002-9667-2244>
 Jean-Baptiste Ruffio  <https://orcid.org/0000-0003-2233-4821>
 Dmitry Savransky  <https://orcid.org/0000-0002-8711-7206>
 Adam C. Schneider  <https://orcid.org/0000-0002-6294-5937>
 Anand Sivaramakrishnan  <https://orcid.org/0000-0003-1251-4124>
 Rémi Soummer  <https://orcid.org/0000-0003-2753-2819>
 Sandrine Thomas  <https://orcid.org/0000-0002-9121-3436>
 Kimberley Ward-Duong  <https://orcid.org/0000-0002-4479-8291>

References

- Arnold, J. A., Weinberger, A. J., Videen, G., & Zubko, E. S. 2019, *AJ*, **157**, 157
- Asensio-Torres, R., Janson, M., Hashimoto, J., et al. 2016, *A&A*, **593**, A73
- Augereau, J. C., Lagrange, A. M., Mouillet, D., Papaloizou, J. C. B., & Grorod, P. A. 1999, *A&A*, **348**, 557
- Bailey, V. P., Poyneer, L. A., Macintosh, B. A., et al. 2016, *Proc. SPIE*, **9909**, 99090V
- Baraffe, I., Chabrier, G., Barman, T., Allard, F., & Hauschildt, P. 2003, *A&A*, **402**, 701
- Bentley, M. S., Schmied, R., Mannel, T., et al. 2016, *Natur*, **537**, 73
- Bhowmik, T., Boccaletti, A., Thébault, P., et al. 2019, *A&A*, **630**, A85
- Boccaletti, A., Augereau, J.-C., Lagrange, A.-M., et al. 2012, *A&A*, **544**, A85
- Brown, A., Vallenari, A., Prusti, T., et al. 2018, *A&A*, **616**, A1
- Burrows, C. J., Krist, J. E., Stapelfeldt, K. R., & WFPC2 Investigation Definition Team 1995, AAS Meeting, **187**, 32.05
- Canovas, H., Ménard, F., de Boer, J., et al. 2015, *A&A*, **582**, L7
- Cataldi, G., Wu, Y., Ohashi, N., et al. 2020, *ApJ*, **892**, 99
- Currie, T., Rodrigues, T. J., Debes, J., et al. 2012, *ApJ*, **757**, 28
- De Rosa, R. J., Nguyen, M. M., Chilcote, J., et al. 2020, *JATIS*, **6**, 015006
- Debes, J. H., Weinberger, A. J., & Kuchner, M. J. 2009, *ApJ*, **702**, 318
- Dohnanyi, J. 1969, *JGR*, **74**, 2531
- Donaldson, J., Lebreton, J., Roberge, A., Augereau, J.-C., & Krivov, A. 2013, *ApJ*, **772**, 17
- Draine, B. T. 1985, *ApJS*, **57**, 587
- Draine, B. T., & Lee, H. M. 1984, *ApJ*, **285**, 89
- Draper, Z. H., Duchêne, G., Millar-Blanchaer, M. A., et al. 2016, *ApJ*, **826**, 147
- Droettboom, M., Caswell, T. A., Hunter, J., et al. 2017, Matplotlib/matplotlib v2.0.2, Zenodo, doi:10.5281/zenodo.573577
- Engler, N., Schmid, H. M., Thalmann, C., et al. 2017, *A&A*, **607**, A90
- Esposito, T. M., Duchêne, G., Kalas, P., et al. 2018, *AJ*, **156**, 47
- Esposito, T. M., Fitzgerald, M. P., Graham, J. R., & Kalas, P. 2014, *ApJ*, **780**, 25
- Esposito, T. M., Kalas, P., Fitzgerald, M. P., et al. 2020, *AJ*, submitted
- Fitzgerald, M. P., Kalas, P. G., & Graham, J. R. 2007, *ApJ*, **670**, 557
- Foreman-Mackey, D. 2016, *JOSS*, **24**, 1
- Foreman-Mackey, D., Hogg, D. W., Lang, D., & Goodman, J. 2013, *PASP*, **125**, 306
- Fratini, E., Muñoz, O., Moreno, F., et al. 2019, *MNRAS*, **484**, 2198
- Graham, J. R., Kalas, P. G., & Matthews, B. C. 2007, *ApJ*, **654**, 595
- Greaves, J. S., Holland, W. S., Matthews, B. C., et al. 2016, *MNRAS*, **461**, 3910
- Hedman, M. M., & Stark, C. C. 2015, *ApJ*, **811**, 67
- Hughes, A. M., Duchêne, G., & Matthews, B. C. 2018, *ARA&A*, **56**, 541
- Hung, L.-W., Duchêne, G., Arriaga, P., et al. 2015, *ApJL*, **815**, L14
- Hunter, J. D. 2007, *CSE*, **9**, 90
- Jones, E., Oliphant, T., Peterson, P., et al. 2001, SciPy: Open Source Scientific Tools for Python, <http://www.scipy.org/>
- Kalas, P. 2005, *ApJL*, **635**, L169
- Kalas, P. G., Rajan, A., Wang, J. J., et al. 2015, *ApJ*, **814**, 32
- Kennedy, G. M., Marino, S., Matrà, L., et al. 2018, *MNRAS*, **475**, 4924
- Khare, B. N., Sagan, C., Arakawa, E. T., et al. 1984, *Icar*, **60**, 127
- Kral, Q., Matrà, L., Wyatt, M. C., & Kennedy, G. M. 2017, *MNRAS*, **469**, 521

- Krivov, A., Löhne, T., & Sremčević, M. 2006, *A&A*, **455**, 509
- Lagrange, A.-M., Gratadour, D., Chauvin, G., et al. 2009, *A&A*, **493**, L21
- Lee, E. J., & Chiang, E. 2016, *ApJ*, **827**, 125
- Li, A., & Greenberg, J. M. 1997, *A&A*, **323**, 566
- Li, A., & Greenberg, J. M. 1998, *A&A*, **331**, 291
- Lin, J. W., & Chiang, E. 2019, *ApJ*, **883**, 68
- MacGregor, M. A., Weinberger, A. J., Hughes, A. M., et al. 2018, *ApJ*, **869**, 75
- Macintosh, B., Graham, J. R., Ingraham, P., et al. 2014, *PNAS*, **111**, 12661
- Madurowicz, A., Macintosh, B., Bailey, V. P., et al. 2019, *JATIS*, **5**, 049003
- Maire, J., Perrin, M. D., Doyon, R., et al. 2012, *Proc. SPIE*, **8451**, 84513G
- Maness, H., Fitzgerald, M., Paladini, R., et al. 2008, *ApJL*, **686**, L25
- Marshall, J. P., Maddison, S. T., Thilliez, E., et al. 2017, *MNRAS*, **468**, 2719
- Mazoyer, J., Boccaletti, A., Augereau, J.-C., et al. 2014, *A&A*, **569**, A29
- Millar-Blanchaer, M. A., Graham, J. R., Pueyo, L., et al. 2015, *ApJ*, **811**, 18
- Milli, J., Mouillet, D., Lagrange, A. M., et al. 2012, *A&A*, **545**, A111
- Milli, J., Vigan, A., Mouillet, D., et al. 2017, *A&A*, **599**, A108
- Moerchen, M. M., Telesco, C. M., De Buizer, J. M., Packham, C., & Radomski, J. T. 2007, *ApJL*, **666**, L109
- Oliphant, T. E. 2006, *A Guide to NumPy*, Vol. 1 (Spanish Fork, UT: Trelgol Publishing), <http://numpy.org>
- Olofsson, J., Samland, M., Avenhaus, H., et al. 2016, *A&A*, **591**, A108
- Pérez, F., & Granger, B. E. 2007, *CSE*, **9**, 21
- Perrin, M. D., Duchene, G., Millar-Blanchaer, M., et al. 2015, *ApJ*, **799**, 182
- Perrin, M. D., Ingraham, P., Follette, K. B., et al. 2016, *Proc. SPIE*, **9908**, 990837
- Perrin, M. D., Maire, J., Ingraham, P., et al. 2014, *Proc. SPIE*, **9147**, 91473J
- Perryman, M. A. C., Lindegren, L., Kovalevsky, J., et al. 1997, *A&A*, **500**, 501
- Pinte, C., Ménard, F., Duchêne, G., & Bastien, P. 2006, *A&A*, **459**, 797
- Pollack, J. B., & Cuzzi, J. N. 1980, *JAtS*, **37**, 868
- Pollack, J. B., Hollenbach, D., Beckwith, S., et al. 1994, *ApJ*, **421**, 615
- Poyneer, L. A., De Rosa, R. J., Macintosh, B., et al. 2014, *Proc. SPIE*, **9148**, 91480K
- The Astropy Collaboration, Price-Whelan, A. M., Sipőcz, B. M., et al. 2018, *AJ*, **156**, 123
- Redfield, S. 2007, *ApJL*, **656**, L97
- Ren, B., Pueyo, L., Ben Zhu, G., Debes, J., & Duchêne, G. 2018, *ApJ*, **852**, 104
- Rodigas, T. J., Debes, J. H., Hinz, P. M., et al. 2014, *ApJ*, **783**, 21
- Rodigas, T. J., Stark, C. C., Weinberger, A., et al. 2015, *ApJ*, **798**, 96
- Schmid, H. M., Joos, F., & Tschan, D. 2006, *A&A*, **452**, 657
- Schneider, G., Grady, C. A., Hines, D. C., et al. 2014, *AJ*, **148**, 59
- Schneider, G., Silverstone, M. D., & Hines, D. C. 2005, *ApJL*, **629**, L117
- Shen, Y., Draine, B., & Johnson, E. T. 2009, *ApJ*, **696**, 2126
- Silverstone, M. D. 2000, PhD thesis, Univ. California, Los Angeles
- Smith, B. A., & Terrile, R. J. 1984, *Sci*, **226**, 1421
- Soummer, R., Pueyo, L., & Larkin, J. 2012, *ApJL*, **755**, L28
- Tamura, M., Fukagawa, M., Kimura, H., et al. 2006, *ApJ*, **641**, 1172
- Thebault, P. 2009, *A&A*, **505**, 1269
- Thebault, P., & Augereau, J. C. 2007, *A&A*, **472**, 169
- Thebault, P., Kral, Q., & Augereau, J.-C. 2014, *A&A*, **561**, A16
- Wang, J. J., Rajan, A., Graham, J. R., et al. 2014, *Proc. SPIE*, **9147**, 914755
- Wang, J. J., Ruffio, J.-B., De Rosa, R. J., et al. 2015, pyKLIP: PSF Subtraction for Exoplanets and Disks, V2.0, Astrophysics Source Code Library, [ascl:1506.001](https://ui.adsabs.org/abs/2015ascl..1506.001)
- Wyatt, M. C. 2008, *ARA&A*, **46**, 339
- Zubko, V. G., Mennella, V., Colangeli, L., & Bussoletti, E. 1996, *MNRAS*, **282**, 1321